UCLA

UCLA Electronic Theses and Dissertations

Title

Transverse-Sheet Illumination Microscopy

Permalink

https://escholarship.org/uc/item/3kd6d6kr

Author

Carmona, Javier

Publication Date

2021

Peer reviewed|Thesis/dissertation

eScholarship.org Powered by the California Digital Library
University of California

UNIVERSITY OF CALIFORNIA
Los Angeles

Transverse-Sheet Illumination Microscopy

A thesis submitted in partial satisfaction
of the requirements for the degree
Master of Science in Electrical and Computer Engineering

by

Javier Carmona Jr

2021

© Copyright by
Javier Carmona Jr
2021

ABSTRACT OF THE THESIS

Transverse-Sheet Illumination Microscopy

by

Javier Carmona Jr
Master of Science in Electrical and Computer Engineering
University of California, Los Angeles, 2021
Professor Katsushi Arisaka, Chair

If we are to understand how nature formulates complex animal behavior, we must develop the tools that have the capabilities to capture these processes in their full capacity. I have created Transverse-Sheet Illumination Microscopy (TranSIM), a highly customizable, single objective microscope, with micron level resolution (0.7 μm, 1.1 μm, 1.6 μm in x, y, and z, respectively) with the ability to image extended three dimensional volumes (750 μm x 560 μm x 160 μm) at 200 volumes per second. For *Danio rerio*, approximately 10^5 neurons were imaged in 3D, opening an unparalleled view into the animal's complex processes at near millisecond temporal resolution. Fast intra-planar and inter-planar processes were observed signaling that utility of TranSIM. Overall, a 10-fold increase in the total volumetric imaging rate is achieved compared to any system currently available, and still with ample room for improvement.

The thesis of Javier Carmona Jr is approved.

Aydogan Ozcan

Peyman Golshani

Katsushi Arisaka, Committee Chair

University of California, Los Angeles

2021

To my mother, father, and siblings . . .
for this achievement belongs to us all!
. . .
I will never forget the sacrifices you all
made so that I can be where I am now.

TABLE OF CONTENTS

1 Introduction . . . 1

1.1 Motivation . . . 1

2 Fluorescence Microscopy Principles . . . 5

2.1 Fluorescence Microscopy . . . 5

2.2 Spatial Resolution and Numerical Aperture . . . 8

3 Spatiotemporal Advancements in Microscopy . . . 11

3.1 Reasoning . . . 11

3.2 Confocal Microscopy . . . 11

3.2.1 Spinning Disk Confocal Microscopy . . . 14

3.2.2 Line-Scanning Confocal Microscopy . . . 15

3.3 Light-Sheet Microscopy . . . 16

3.4 Scanned Volumetric Imaging . . . 19

3.5 Static Volumetric Imaging . . . 20

3.5.1 Light Field Microscopy . . . 20

3.5.2 SCAPE Microscopy . . . 21

3.5.3 Deep-Z Microscopy . . . 23

3.5.4 Transverse-Sheet Illumination Microscopy . . . 25

3.6 Volumetric Rates and Bandwidth . . . 26

4 Methods . . . 28

4.1 Optical Design . . . 28

4.1.1 Beam Multiplexing . . . 31

4.1.2 Plane Separation and Focal Plane Readjustment 33

4.2 Data Acquisition and Control 36

4.2.1 Synchronization Waveforms 36

4.2.2 Hardware Control 40

5 Results 41

5.1 Spatial Resolution 41

5.1.1 Lateral and Axial Resolution 41

5.1.2 Resolution Depth Dependence 44

5.2 Photon Efficiency 46

5.3 Melanoma Cells Imaging 48

5.4 *Caenorhabditis elegans* Imaging 50

5.5 *Danio rerio* Imaging 53

5.5.1 Intra-planar Neural Signal Propagation. 57

5.5.2 Inter-planar Neural Signal Propagation 59

6 Future Directions 62

6.1 Behavioral Observation 62

6.2 Virtual Reality 63

6.3 Improved Illumination 64

6.4 Deep-Z Application 66

6.5 Genetically Encoded Voltage Indicators 67

7 Discussion and Conclusion 69

References 71

LIST OF FIGURES

1.1 *4D Space-Time Diagram of Organisms.* The 3D volume of the brain is condensed into a single logarithmic dimension, the y-axis, while time is on the x-axis. Starting at millisecond temporal processes, which are the typical domain of action potentials, up to high level processes like learning adaptation and education, which can take on the order of days to years. In a single spatial dimension, a synapse occupies a region on the order of a 100's of nanometers, up to high level human brains which are on the order of 10's of centimeters. The total number of neurons and neural connections are shown per animal. To record the entire brain, the number of "digits" refers to the total orders of magnitude required in voxels to address record the organism. For example, a *C. elegans* brain occupies 3 orders of magnitude, from synapse to entire brain, in space over 3 dimensions, at 10 millisecond resolution over the span of a few days (10^7, order 7), equating to a total voxel requirement of order 16 for a full recording. Courtesy of Dr. Katsushi Arisaka. Adopted from TranSIM NIH R21 grant proposal depicting the space-time occupation of organisms[1]. 2

1.2 *Microscopy 4D Scanning Comparison.* Critical areas of Neuroscience research lie in the study of action potentials/brain waves and large volumetric regions in the brains of organisms. Highlighted in grey are advancements in microscopy have lead to a large exploration in the 4D occupation of brains. *Transverse-Sheet Illumination Microscopy* reaches highly sought regions of exploration in terms of *volume* and *speed*, increasing the total volumetric field of view up to near 1 mm^3, while achieving rates comparable to the fastest methods available, commercially and otherwise, with further room for improvement. For comparison, four regions indicating state-of-the-art research indicate a (1) $\sim$0.1 mm^3 region scanned at 0.8 volumes per second (VPS), Ahrens et al. (2013) [2], fastest volumetric scans; (2) $\sim$0.017 mm^3 at 10 VPS, and (3) $\sim$0.005 mm^3 at 321 VPS, Voleti et al. (2019) [3], and (4) fastest sub-micron resolution, Ahrens et al. (2013) [2] and Chen et al. (2014) [4]. TranSIM was tested up to $\sim$0.07 mm^3 at 200 VPS for a 5 minute period, denoted by the blue rectangle. The blue dashed line indicates the cut-off boundary that TranSIM can operate by changing the volumetric scanning parameters (slowing the scan rate, increasing the volume rate, or vice versa). . . 4

2.1 *Jablonski Transition Diagram.* In a fluorescent microscopy, fluorescent proteins or molecules are excited (denoted by the excitation photons) which force the molecule to undergo an electronic transition from the ground state energy level, E_0, to an excited energy state, E_2 or E_1, denoted by the bold thick lines. The incoming photon might elevate the electrons to a slightly higher energy state than the bare excited states, called vibrational states (light thin lines). If this occurs, a few processes occur to bring the excited electron down to the first excited energy ground vibrational state, E_1, namely, vibrational relaxation and internal conversion. Upon reaching the ground vibrational state of the first excited state, the electron transitions to a ground energy state. In the process a photon is emitted with equivalent energy to the transition, $h\nu_{em}$. Any remaining energy is dissipated through non-radiative means until E_0 is achieved. 6

2.2 *Schematic of Epi-Fluorescent Microscope and Band-Pass Filtering Regions.* A broadband (white) light source is filtered around the peak excitation wavelength. The long-pass dichroic mirror reflects the filtered light into the objective and the condenser focuses the light onto the back focal plane of the objective to produce an even illumination field at the sample plane. After illumination, the sample undergoes fluorescence and light is captured back through the objective, usually mixed with scattered excitation light. The long-pass dichroic mirror allows the higher wavelength light through and remnant excitation light and other undesirable light are rejected using an emission band-pass filter. (Excitation/Emission spectra retrieved from Chroma Technology Corporation, Bellows Falls, VT USA) 8

2.3 *Airy Disk Formation.* From equation 3.8, the field intensity produces an Airy disk pattern, where the central lobe contains most of the intensity. When there are multiple Airy disks adjacent to one another, the limit by which they can be differentiated is when their distance is at least $ka\omega = 1.220\pi$, or the distance to the first zero of the function. 9

3.1 *Point Confocal Microscopy.* Invented by Marvin Minsky, in 1957, the point confocal microscope clarified a fuzzy Widefield traditional method by rejecting out of focus light. 12

3.2 *Widefield vs. Confocal Comparison.* By placing a pinhole at approximately half the distance to the first dark lobe, the overall lateral resolution of the system can be increase by a factor of 2 while retaining nearly of the input intensity. The solid line indicates what a widefield system would see. The dashed red line indicates the compression of the first lobe down by a factor of 2 after applying a confocal pinhole. 14

3.3 *Line-Scanning Confocal Microscopy.* By focusing light down to a line using a cylindrical lens, that scanning of that line can be synchronized with the rolling shutter of modern sCMOS cameras. The net effect is a system that is half widefield and have confocal. In the direction of the shutter, confocality exists whereby the rolling shutter rejects out of focus light, while in the orthogonal direction, widefield is present. 15

3.4 *Light Sheet Microscopy.* Conventional light-sheets (*left*) are created using a cylindrical lens to focus the light only in one dimension. To create "pencil-like" beams, *right* that are instead scanned confocally with the rolling sCMOS sensor, the methodology is to use a regular spherical lens, rather than a cylindrical lens. . . 17

3.5 *Comparison of Light-Sheet Illumination Beams.* The first and standard beam illumination method is created using a cylindrical lens which collapses a gaussin plane wave in one dimension. The typical propagation length is 100-500 μm, however this type of beam does not afford any confocality application to a rolling shutter sCMOS sensor. For confocality, a spherical lens can be used which collapses the beam in both dimensions with the same propagation distance. Non-diffracting beams created by interference, Bessel-Gauss beams, have a much larger propagation distance, 250-1000 μm, compared to same numerical aperture collapsed Gaussian Beams. With the aid of a Spatial Light Modulator (SLM), an array of Bessel beams can be configured to interfere even further by trimming away at each adjacent beams thereby reducing the overall waist of the beams. Courtesy of Blake Madruga, adopted from his Thesis work on Configurable Bessel-Gaussian Sheet Illumination Microscopy[5]. 18

3.6 *3-Dimensional Scanning.* Two main methods for mechanic depth scanning are the translation of the objective using a piezoelectric actuator (left) and movement of the sample stage using a motorized stage (right). 19

3.7 *SCAPE Microscopy.* With a single objective, SCAPE microscopy achieves depth resolved images. To do so, an oblique illumination sheet is implemented. On the detection axis, only the orthogonal directional fluorescence is utilized. After descanning, the descanned plane, is relayed to a secondary objective whereby utilizing a tertiary, the image plane is mapped onto a flat image plane and onto an imaging sensor. 22

3.8 *Deep-Z Microscopy.* Single plane images are feed into a trained neural network, where the are refocused up to distance of $\pm 10\mu$m. For conformation, the Deep-Z generated refocused images are compared to the mechanical translations focused images for a fluorescent bead (a). (b) is distribution of the FWHM of 300 nm fluorescent beads in the lateral dimension for both Deep-Z propagation and mechanical objective translation. Similarly for (c), the axial dimension FWHM are measure. In both cases, it is seen that the Deep-Z propagation matches very well with the mechanical translation. 24

4.1 *Schematic of Transverse-Sheet Illumination Microscopy.* 29

4.2 *Laser Line Beam Multiplexing.* To create a 9 imaging planes with laser line focus, a single laser line created using a cylindrical lens is reflected an angle, θ, to the normal of depth refection mirror. The light then travels to a 90:10 broadband beamsplitter (BS), where 90% of the light is reflect back onto the mirror at angle angle θ and 10% is transmitted. The process continues ad infinitum; for the purposes of TranSIM, 9 useful beams are ultilized. Each reflection beam created has 10% of the previous reflection, therefore, the intensities of the beams decay by power law. To increase the later separation y, the angle θ can be adjusted. To increase the depth separation, the distance, d can be increase. The only requirement is that the beamsplitter and depth reflection mirrors maintain a parallel geometry, otherwise the beams will begin diverge. 32

4.3 *Plane Separation.* After injection into the cyclic apparatus, the beams now undergo separation. To separate the planes, the beams are focused down to an image where they retain have axial and lateral separation. Using a knife-edge mirror, a single image plane can be reflected into the imaging sensor and the remaining planes are allowed to continue undisturbed. 33

4.4 *End of Cycle Readjustment Process.* After the first cycle, image field would return to the same location as when it started the cycle. Using the last telecentric relay unit, the planes can be refocused axially and readjusted laterally to remap the adjacently the previous cycle. (A) shows how to laterally translate (in Y-dimension) by taking the telecentric unit and moving is uniformly until the image field returns to a centered position as if the first of the remaining image planes were the first true image plane. Similarly, to move offset in the X-dimension, such that the planes pass underneath the D-shaped mirror, the telecentric relay unit it moved uniformly until the there is enough clearance. (B) For depth, only the last telecentric lens is adjusted such that the image planes are focused to overlap the planes the planes of the previous cycle. 35

4.5 *Synchronization Waveforms.* Three Hamamatsu Flash 4.0 V2s are synchronized by a parallel TTL signal. The field scanning galvanometer has a smoothed out sawtooth waveform. On the reset travel time, the camera's undergo readout. The image field is de-scanned due to the backward propagation through the detection arm onto the scanning galvo. After plane rearrangement, the image planes are rescanning using the camera located galvanometers. TranSIM allows for 1-dimensional spatiotemporal compression (similar to point confocal systems whereby the scan range determines the magnification) by expanding or contracting the amplitude of the scanning galvo while maintaining the camera galvo-camera line-scanning matched. Lower and upper boundaries denoted by dashed lines correspond to 0.25X and 2X magnification, respectively, for demonstrative purposes. 38

4.6 *Detailed Synchronization Waveform Regions.* The period begins with the camera being externally start triggered to light-sheet scanning such that it coincides with the linear scan region of the galvanometers. After completing the scan, the camera reads out to the data acquisition computer via a camera link frame grabber and the galvanometers are reset. This reset process incorporates the flyback process and acceleration back produce a linear scan region for the subsequent period. . . 39

4.7 *Wiring Schematic of Microscope.* Platform sTR4 Socket Threadripper 1950X CPU (Advanced Micro Devices, Santa Clara, CA, USA) workstation. Analog signals are created an NI PCIe-6363 multifunction I/O device. For camera control, a parallel TTL signal sent to three Hamamatsu Flash 4.0 V2s via AO0. The external start trigger activates the rolling shutter (light-sheet mode) of the sCMOS sensor which is synchronized with the "camera" and "scanning" galvanometers linear scan regions. The resulting image is captured via three FireBird Camera Link Frame Grabbers (1xCLD-2PE8) and sent to independent Samsung 970 PRO NVMe SSDs. AO2 controls the field scanning galvanometer with variable amplitude. AO1 sends scan signal to three camera galvanometers. 3-dimensional motorized stage is connected in series for each dimension along with a joystick connected to the computer via USB for software control. One of the camera galvo's, the scanning galvo, and the TTL signal sent to the cameras are monitored via the analog inputs (AI0-AI2). 40

5.1 *Point Spread Function Theoretical vs Experimental.* After reaching the plane adjustment cycle, a comparison between the first image plane and the theoretical point spread functions is made. On the *left* the theoretical PSF generated using the Born and Wolf optical model using the ImageJ Plugin: PSF Generator by the EPFL Biomedical Imaging Group[6]. On the *right* is the average PSF of 100 nm fluorescent beads imaged image under 488 nm excitation. To obtain an average, beads were image using a Nikon 40X 0.8 NA objective. A Gaussian profile was fit to the intensity. 43

5.2 *Point Spread Function Depth Dependence.* 9 total image planes were imaged onto 3 separate sCMOS cameras. Due to the cyclic rearrangement and image relay process, the point spread function is bound to increase as a function of number of relays. For the 9 images planes, image resolution in all 3 dimensions had a linear relation to imaged depth. Reconstructed averages of the PSF in XY and XZ projections are displayed as a function of "increasing depth" or conversely, the number of increasing relays the image has undergone from left to right. . . . 44

5.3 *Plane Dependence Spatial Resolution.* 100 nm fluorescent microspheres were imaged to determine the change in spatial resolution as a function of imaged plane. The imaging objective was a Nikon CFI Apo NIR 40X W, with an NA of 0.8. There is a linear dependence on the spatial resolution of the system and planes for all dimensions. Due to the confocality of the system, the least varying resolution is found in the x-dimension, with overall submicron resolution obtained. The y-dimensions shows a slightly larger over resolution and the function has an overall larger increase as a function plane. The axial dimension, z, also an increasing dependence on plane with the best axial resolution occurring at the initial plane. 45

5.4 *TranSIM Photon Efficiency.* On the left, the calculated normalized intensity produced by illumination beam multiplexing, relay unit loss, and the overall theoretical normalized intensity at the image sensors. On the right, the measured normalized intensity at the sample, and at the image sensors, compared to the theoretical normalized intensity at the sensors. Note that the measured intensities at the sensor deviate from the theoretical, but this can be attributed to the fact that the illumination intensities did not follow the theoretical and began to decay faster after the fifth image plane. 47

5.5 *GFP Tagged Melanoma Cells.* Each plane has an axial spatial separation of 20 μm and imaged using a Nikon 16X CFI LWD Plan Fluorite Objective, 0.80 NA objective with an effective magnification of 8X. NAOMM-1-GFP human uveal melanoma cells, which endogenously express GFP in the cytoplasm, were received from Dr. Samar Alsafadi of Curie Institute (Paris). Cells were maintained in RPMI 1640 (Gibco 21875-034) containing 10% fetal bovine serum and 1% Pen-Strep (Gibco 15140-122), on poly-d-lysine coated dishes in a 37°C, 5% CO$_2$ incubator. Cells were fixed for 20 minutes with 4% paraformaldehyde at 40$\tilde{7}$0% con-fluency, leaving space to spread the cells into uniquely identifiable XY positions. Following fixation, cells were rinsed with and kept in 1x PBS. 49

5.6 *GCaMP3 Encoded C. elegans.* Ca^{2+} indicator expresses in the muscles highlighted by bright fluorescence on the walls of the nematode. Single time frame. Captured at 200 HZ. Samples courtesy of Dr. Pavak Shah UCLA. 51

5.7 *3D Render of C. elegans.* Single volume rendition created in ClearVolume, Royer et al. (2015)[7]. Samples courtesy of Dr. Pavak Shah UCLA. 52

5.8 *GCaMP6s Encoded Danio Rerio 1.* Each plane has an axial spatial separation of 40 μm and imaged using a Nikon 16X CFI LWD Plan Fluorite Objective, 0.80 NA objective with an effective magnification of 8X. The voluemtric rate of imaging is 200 VPS with a field of view per image plane of 554 μm × 374 μm. The fish was held in place for imaging using a 2.5% by volume agarose mixture for near refractive index matching imaging. In addition, most of the agarose that lie on top of the brain region was removed as to reduce the agarose layer excitation and emission light had to travel through. 54

5.9 *GCaMP6s Encoded Danio Rerio. 2* Each plane has an axial spatial separation of 40 μm and imaged using a Nikon 16X CFI LWD Plan Fluorite Objective, 0.80 NA objective with an effective magnification of 8X. The voluemtric rate of imaging is 200 VPS with a field of view per image plane of 554 μm × 374 μm. The fish was held in place for imaging using a 2.5% by volume agarose mixture for near refractive index matching imaging. In addition, most of the agarose that lie on top of the brain region was removed as to reduce the agarose layer excitation and emission light had to travel through. 55

5.10 *Mustard Oil Induced Neural Activation of Danio rerio.* In order to induce substantial brain activity, mustard oil, an irritant, was injected into the water reservoir where the fish was held in place using an agarose bed. On the *left*, is a snap shot of the pre-mustard oil neural activity. On the *right*, mustard oil induced neural activation can be seen by higher overall signal strength. Recreation of experiment done by Roberts et al (2020)[8] 56

5.11 *Neural Signal Propagation in Danio rerio.* Imaged at 200 VPS, the single image plane was analyzed to show signal propagation. 4 locations were chosen from visual inspection of neural activation. Analysis shows that the signal propagates inwards from the Neurophil (NP) to the Periventricular Layer (PVL). The spatial separation of each location is 40 μm. Temporal sequence shows that from the first location inside the NP to the central PVL location, there is a ∼100 ms delay in the leading edge activation. The wavefront propagation speed was measured to be 1200 μm/s. 58

5.12 *Temporal Sequence at Various Depths.* The volumetric imaging rate is 200 VPS, resulting in a temporal resolution of 5 ms. Each plane shown is 40 μm apart. Overall signal from the three regions of interest are plotted in the top graph. Areas of interest indicated by their time frames are plotted below. Leading and falling edge signals indicate a temporal dependence from plane to plane. 60

5.13 *Multi-plane Ca^{2+} Wave Propagation.* Three independent planes are shown spaced 40 μm apart, corresponding to the 1^{st}, 3^{rd}, and 5^{th} image planes in the volume. Starting from the left column, at t = 0 ms, the wave begins at the top of each plane and propagates downward towards to tail of the fish, in the span of 80 ms, inducing a tail bout. 61

6.1 *Zebrafish Eye Tracking Software.* Custom real-time eye tracking software made in LabVIEW. Maximum operational eye tracking speed determined by sensor. Angular resolution of $\leq 0.5^{o}$. Tested at frames rates of up to 550 FPS with Allied Vision Mako U-029B USB 3.0, monochrome camera, at full frame, 640 pixels × 480 pixels. 63

6.2 *Proposed Illumination. Transverse-Sheet Illumination Microscopy* has in its current design, a single Gaussian sheet illumination mechanism, multiplexed 9 times. These multiplexed beams have a broad colliding angle, which in turn causes phototoxicity and photobleaching at the sample. To reduce said effects, two additional illumination methods are proposed in order to clear as much of the area being illuminated from light contamination. On the *left*, is a double Gaussian sheet method by which to collide nearly orthogonal sheets to a single location thereby clearing the sample light contamination from the top and bottom of the collision location. On the *right*, is an increased depth illumination method and create a long uniform illumination sheet similar to those created in Bessel-Gauss Light Sheet Microscope by plane wave interference. 65

6.3 *TranSIM with Deep-Z Propagation.* Due to the limited number of layers *TranSIM* can reliably capture, there is a trade-off between layer separation and total one wishes to image. However, both cannot be improved simultaneously. Instead, Deep-Z, a new depth refocusing microscopy method sheds light on the possibility of instead optimizing the axial separation and turning to neural networks to regain the out of focus/plane information and recreate a true 3D volume. 67

LIST OF TABLES

3.1 *Microscope Comparison.* Entire parameter space of various microscopes are listed in the area of volumetric scanning. Major research developments in microscopy have taken place in order to increase the speed are which they can image volumes. Although their suitable application domains vary wildly from system to system, the overarching connection is *bandwidth.* In the *grey* column, the total bandwidth of the system is shown in units of GigaPixels/s. Moreover, the *green* column bypasses any sensor non-equivalences, and instead focuses on the total volumetric imaging field imaging rate that is achieved in mm^3/s, or volume size times the volume rate, of each system. Also shown, are proposed versions of *Transverse-Sheet Illumination Microscopy*, in addition to its first proof-of-concept. These future additions aim to explore the possibility of increased throughput of the system, limited only by the bandwidth of the current imaging sensors. Courtesy of Dr. Arisaka, adopted microscope comparison in NIH R21 Proposal to include experimental results of TranSIM[1]. 27

ACKNOWLEDGMENTS

Katsushi Arisaka ... For going above and beyond your duty as a mentor. The path I lead is largely due to your commitment always making sure I never gave up. Now, I can express myself through my work. Thank you.

Laurent Bentolila ... For being there in a professional and personal manner. Allowing me to roam CNSI and see all the great things people can achieve gave me inspiration.

Aydogan Ozcan ... For taking the time to read my work, your vast contributions, and future possibilities.

Peyman Golshani ... For you assistance and the great work you do for society.

Blake Madruga ... For being a friend and an inspiration. Without your work, mine would not have been possible.

Elizabeth Mills ... For you kind friendship and support.

Steve Mendoza ... For helping to create the LabVIEW programs to run these machines and the funny memories.

Adam Roberts ... For the zebrafish samples, scientific knowledge and continued collaboration.

Brian Jeong ... For the countless beads and zebrafish samples, and for helping with data taking and optics alignment.

Rebecca Huang ... For maintaining and making C. elegans samples.

Daniel Fu ... For the photo-taxis experiments that served as a driving force for this microscope.

Ariana Wilner ... For co-authoring the zebrafish eye tracker in Section 6.1.

Joseph Alzagatiti ... For scientific insight into zebrafish and collaboration.

Yuqi Ma ... For zebrafish sample preparations.

Alan Li ... For help with data taking and optical alignment.

LaTeX Formatting ... Thank you to Leslie Lamport, Dorab Patel, Eduardo Krell, Richard B. Wales, and John Heidemann for creating a friendly UCLA thesis template.

CHAPTER 1

Introduction

1.1 Motivation

In contemporary science, microscopy is an indispensable tool used to study biological organisms. For example, major research animals, like *Danio rerio*, have approximately 10^5-10^6 neurons at a larval stage and more than 10^6 once they reach adulthood [9, 10]. With an approximate radius of 10 μm[11], 10^6 neurons occupy a volumetric region spanning 750 μm × 500 μm × 250 μm. In addition to the quantity and their physical occupation in space, the neurons have activation frequency on the order milliseconds to process their world[12]. Therefore, if we are to understand biological organisms in their full complexity, we must develop the tools that allow us to image large volumetric regions encompassing entire brains with millisecond temporal resolution. Figure 1.1 shows the expansive nature of animals' processing center, the brain, in a *4D Space-Time* diagram.

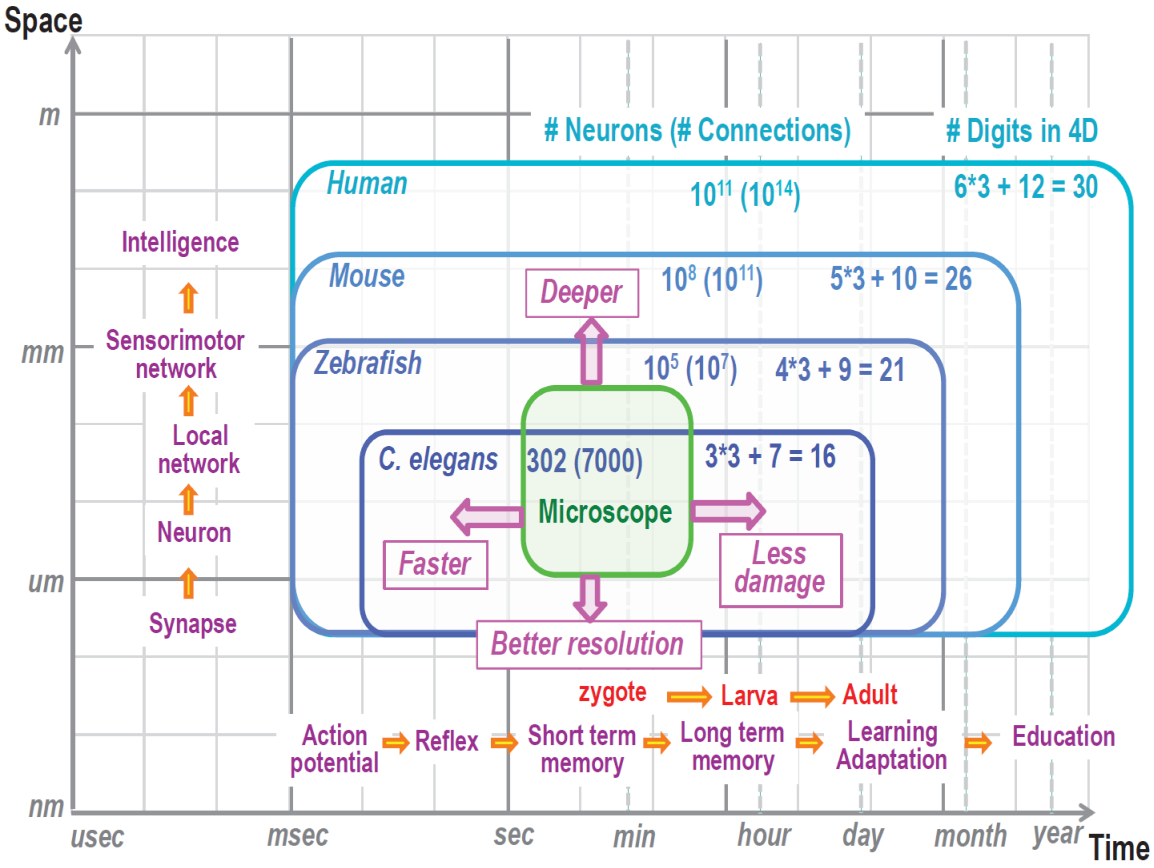
Space
m
mm
um
nm
Intelligence
Sensorimotor network
Local network
Neuron
Synapse
# Neurons (# Connections)
# Digits in 4D
Human
10^{11} (10^{14})
6*3 + 12 = 30
Mouse
Deeper
10^{8} (10^{11})
5*3 + 10 = 26
Zebrafish
10^{5} (10^{7})
4*3 + 9 = 21
C. elegans
302 (7000)
3*3 + 7 = 16
Microscope
Faster
Less damage
Better resolution
zygote
Larva
Adult
Action potential
Reflex
Short term memory
Long term memory
Learning Adaptation
Education
usec
msec
sec
min
hour
day
month
year
Time

Figure 1.1: *4D Space-Time Diagram of Organisms.* The 3D volume of the brain is condensed into a single logarithmic dimension, the y-axis, while time is on the x-axis. Starting at millisecond temporal processes, which are the typical domain of action potentials, up to high level processes like learning adaptation and education, which can take on the order of days to years. In a single spatial dimension, a synapse occupies a region on the order of a 100's of nanometers, up to high level human brains which are on the order of 10's of centimeters. The total number of neurons and neural connections are shown per animal. To record the entire brain, the number of "digits" refers to the total orders of magnitude required in voxels to address record the organism. For example, a *C. elegans* brain occupies 3 orders of magnitude, from synapse to entire brain, in space over 3 dimensions, at 10 millisecond resolution over the span of a few days (10^7, order 7), equating to a total voxel requirement of order 16 for a full recording. Courtesy of Dr. Katsushi Arisaka. Adopted from TranSIM NIH R21 grant proposal depicting the space-time occupation of organisms[1].

Ordinarily, scientists have relied on slow temporal–high spatial resolution techniques like fluorescence microscopy, or alternatively, fast temporal – low spatial resolution local field potential recordings. However, the ultimate goal is to record the activity of the brain in its entirety with fast enough temporal resolution to disambiguate the processes that are happening. By doing so, the question of how animals sense, integrate, and produce motion can be answered at one fell swoop or at least be a step towards the answer. For this reason, I have dedicated my work to designing *Transverse-Sheet Illumination Microscopy*, a system that covers the missing phase space in brain activity recording. In addition, I have created in such a way that it will allow for peripheral systems, like virtual reality, behavioral recording, and other commonly applied systems, due to the single objective geometry. In Figure 1.2, an additional *4D Space-Time* diagram shows the additional phase space that *Transverse-Sheet Illumination Microscopy* covers.

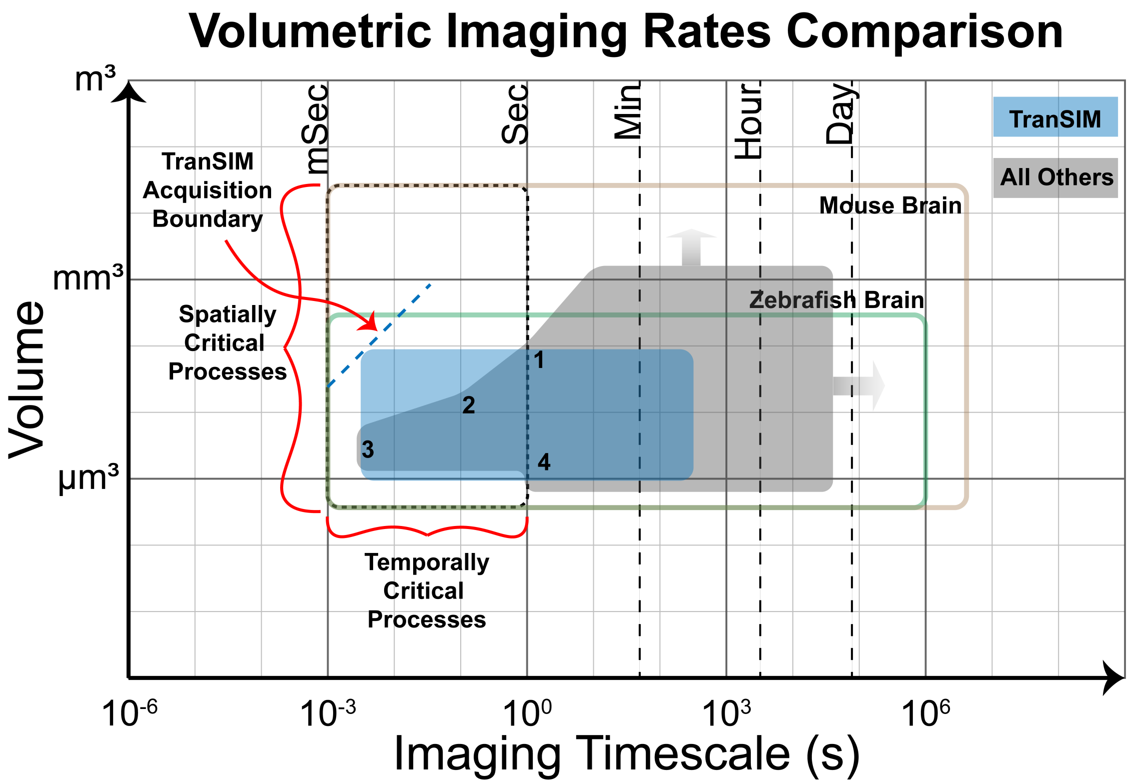

Figure 1.2: *Microscopy 4D Scanning Comparison.* Critical areas of Neuroscience research lie in the study of action potentials/brain waves and large volumetric regions in the brains of organisms. Highlighted in grey are advancements in microscopy have lead to a large exploration in the 4D occupation of brains. *Transverse-Sheet Illumination Microscopy* reaches highly sought regions of exploration in terms of *volume* and *speed*, increasing the total volumetric field of view up to near 1 mm^3, while achieving rates comparable to the fastest methods available, commercially and otherwise, with further room for improvement. For comparison, four regions indicating state-of-the-art research indicate a (1) ∼0.1 mm^3 region scanned at 0.8 volumes per second (VPS), Ahrens et al. (2013) [2], fastest volumetric scans; (2) ∼0.017 mm^3 at 10 VPS, and (3) ∼0.005 mm^3 at 321 VPS, Voleti et al. (2019) [3], and (4) fastest sub-micron resolution, Ahrens et al. (2013) [2] and Chen et al. (2014) [4]. TranSIM was tested up to ∼0.07 mm^3 at 200 VPS for a 5 minute period, denoted by the blue rectangle. The blue dashed line indicates the cut-off boundary that TranSIM can operate by changing the volumetric scanning parameters (slowing the scan rate, increasing the volume rate, or vice versa).

CHAPTER 2

Fluorescence Microscopy Principles

2.1 Fluorescence Microscopy

First described in 1852, by Sir George Gabriel Stokes [13], he noted that some materials have the capability of absorbing radiation and emitting radiation back at a lower frequency, described by the transitions,

$$E_0 + h\nu_{ex} \rightarrow E_{\mathrm{n}} \tag{2.1}$$

$$E_{\mathrm{n}} \rightarrow E_1 \tag{2.2}$$

$$E_1 \rightarrow E_0 + h\nu_{em} \tag{2.3}$$

where, $h\nu_{ex}$, is the energy of the excitation photon, and $h\nu_{em}$, is the energy of the emission photon. See Figure 2.1. The difference in energy between the excitation and emission photon energies is known as the "Stokes' energy shift" and are usually regarded in terms of the peak absorption and emission wavelengths [14, 15].

$$\Delta\lambda = \lambda_{abs} - \lambda_{em} \tag{2.4}$$

Following this principle, microscopy has evolved in such a way as to being able to illuminate the sample of interest with a certain wavelength and recuperate the emission spectra all whilst separable, thereby increasing the contrast if separated[16, 17, 18]. See Figure 2.1.

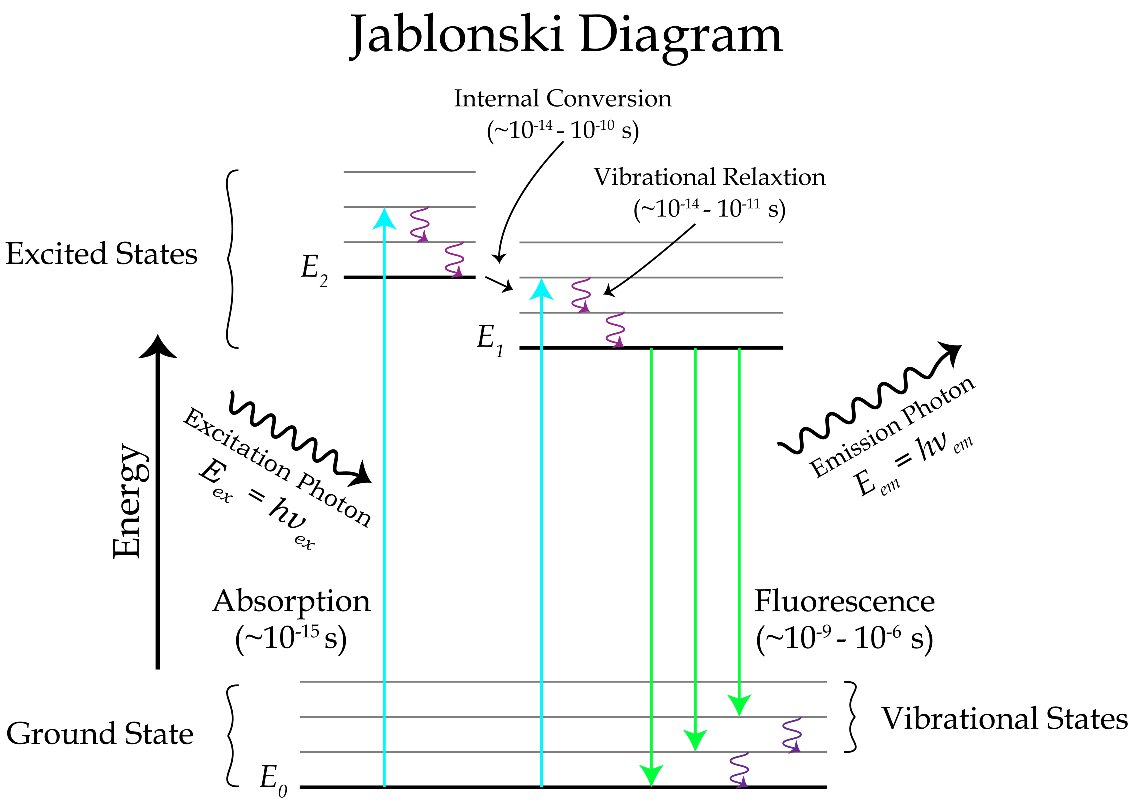
Jablonski Diagram
Internal Conversion
(~10^{-14} - 10^{-10} s)
Vibrational Relaxtion
(~10^{-14} - 10^{-11} s)
Excited States
E_2
E_1
Energy
Excitation Photon
$E_{ex} = h\nu_{ex}$
Emission Photon
$E_{em} = h\nu_{em}$
Absorption
(~10^{-15} s)
Fluorescence
(~10^{-9} - 10^{-6} s)
Ground State
E_0
Vibrational States

Figure 2.1: *Jablonski Transition Diagram.* In a fluorescent microscopy, fluorescent proteins or molecules are excited (denoted by the excitation photons) which force the molecule to undergo an electronic transition from the ground state energy level, E_0, to an excited energy state, E_2 or E_1, denoted by the bold thick lines. The incoming photon might elevate the electrons to a slightly higher energy state than the bare excited states, called vibrational states (light thin lines). If this occurs, a few processes occur to bring the excited electron down to the first excited energy ground vibrational state, E_1, namely, vibrational relaxation and internal conversion. Upon reaching the ground vibrational state of the first excited state, the electron transitions to a ground energy state. In the process a photon is emitted with equivalent energy to the transition, $h\nu_{em}$. Any remaining energy is dissipated through non-radiative means until E_0 is achieved.

More recently, with the discovery of the Green Fluorescent Protein (GFP) by Shimomura et al. (1962) [19, 20], scientists no longer had to stain and possibly damage a biological sample to image it with high contrast. Instead, they could instead could have the organism express the protein and fluoresce naturally. Although GFP is a useful tool to studying biological organisms, the marker was static in time. Meaning, regardless of the dynamic process that were going on in the background where the protein was expressing, the protein only illuminated the scene and created contrast from the microscopists. However, scientist developed the protein even further such that it was now reactive to the dynamic concentrations of calcium ion, Ca^{2+}, giving way to a knew era in fluorescence microscopy, calcium imaging [21]. With GFP and it's Ca^{2+} variants, high contrast imaging can take place that is both safer for the biological sample, while potentially allowing for dynamic processes recording. In Figure 2.2, a schematic of an Epi-Fluorescent microscope and how it takes advantage of the Stoke's Shift produced by GFP and other similar variants.

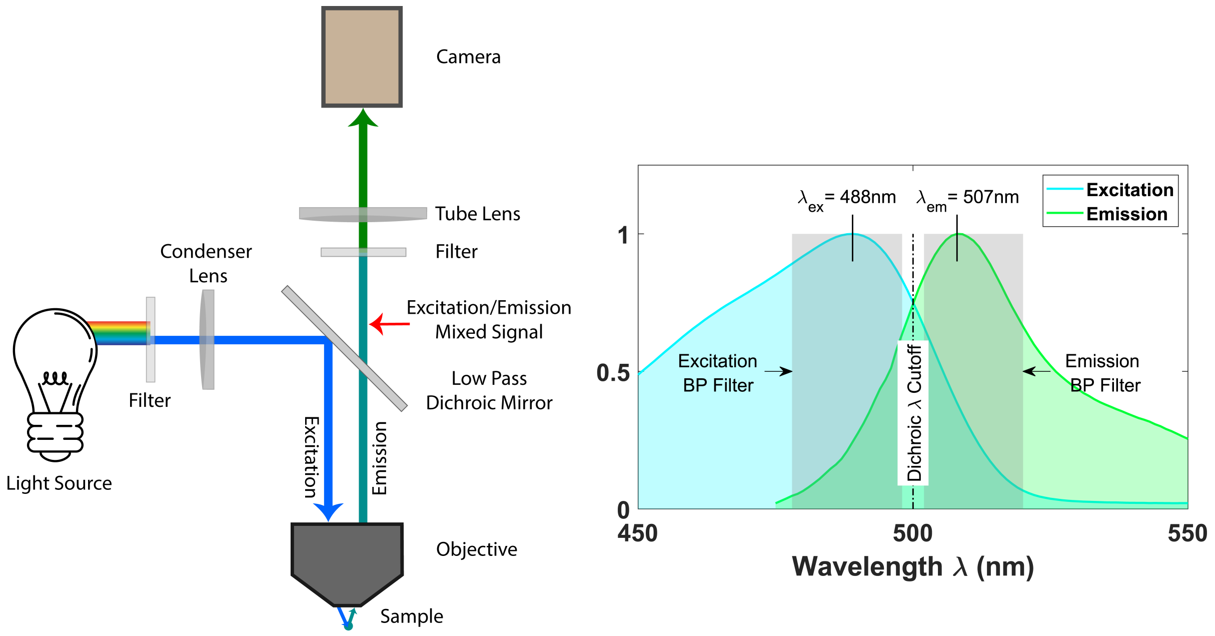
Camera
Tube Lens
Filter
Condenser
Lens
Excitation/Emission
Mixed Signal
Low Pass
Dichroic Mirror
Filter
Light Source
Excitation
Emission
Objective
Sample
λ_{ex} = 488nm
λ_{em} = 507nm
Excitation
Emission
1
0.5
0
Excitation
BP Filter
Dichroic λ Cutoff
Emission
BP Filter
450
500
550
Wavelength λ (nm)

Figure 2.2: *Schematic of Epi-Fluorescent Microscope and Band-Pass Filtering Regions.* A broadband (white) light source is filtered around the peak excitation wavelength. The long–pass dichroic mirror reflects the filtered light into the objective and the condenser focuses the light onto the back focal plane of the objective to produce an even illumination field at the sample plane. After illumination, the sample undergoes fluorescence and light is captured back through the objective, usually mixed with scattered excitation light. The long-pass dichroic mirror allows the higher wavelength light through and remnant excitation light and other undesirable light are rejected using an emission band-pass filter. (Excitation/Emission spectra retrieved from Chroma Technology Corporation, Bellows Falls, VT USA)

2.2 Spatial Resolution and Numerical Aperture

The resolving power of a microscope is due to the *Numerical Aperture*, or NA, of the system. In simple terms, NA is how well a system can collect angular information of the light being capture. The larger the angular capture, the more light that is captured and thus the higher the spatial resolution. A derivation, is covered in greater detail in *Principles of Optics* by Born and Wolf [22]. The resulting intensity profile produced by a field propagating to a far distance, or conversely being focused by an lens, is,

$$I(P) = I_0 \left[\frac{2J_1(ka\omega)}{ka\omega} \right]^2, \tag{2.5}$$

where ω, is a point along the aperture, a, k, is the wave number, and J_1, is a first order Bessel function of the first kind. The intensity is commonly known as an *Airy disk.* See Figure 2.3. In the instance where multiple Airy disks are present, the ideal separation between any 2 disks takes place when the maxima of adjacent disks are located at the first minimum of the first disk. By taking the derivative on the field intensity, we can obtain the zeros of the function where the fist zero occurs at,

$$ka\omega = 1.220\pi. \tag{2.6}$$

Rearranging terms for the dark rings solely in terms of ω, λ, and a, we arrive at, where k is the wavenumber,

$$\omega = 0.610\frac{\lambda}{a}. \tag{2.7}$$

This produces a maximized contrast profile, where the objects are a close as possible, but still discernible from one another. See Figure 2.4.

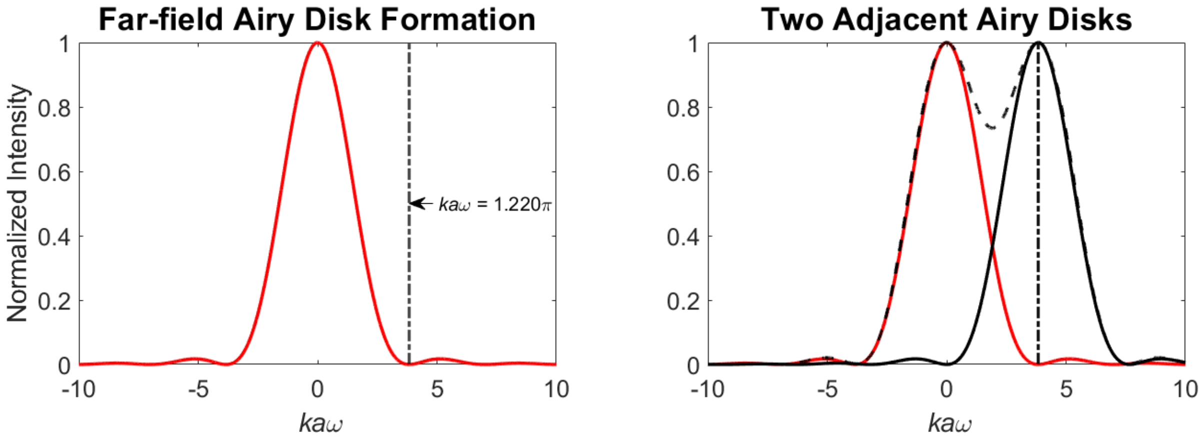

Figure 2.3: *Airy Disk Formation.* From equation 3.8, the field intensity produces an Airy disk pattern, where the central lobe contains most of the intensity. When there are multiple Airy disks adjacent to one another, the limit by which they can be differentiated is when their distance is at least $ka\omega = 1.220\pi$, or the distance to the first zero of the function.

Subsequent difference in ring-to-ring radii converges on the following expression,

$$d_{lateral} = \frac{\lambda}{2a} = \frac{\lambda}{2NA}, \tag{2.8}$$

where, $d_{lateral}$, is the lateral resolution (in the X- and Y-dimensions) of the system, a is the aperture diameter size, λ is the central imaging wavelength, and NA is the numerical aperture when a lens is used. Equation 2.8 is the *diffraction limit* of an imaging system. Similarly, the axial resolution (in the wave propagation direction) has the following relationship to numerical aperture,

$$d_{axial} = \frac{2\lambda}{NA^2}. \tag{2.9}$$

Here it shows that that the axial resolution (Z-dimension) is similarly inversely proportional to the NA of the system, however, also has a quadratic dependence. This is and important factor to take into account, because that signifies that although the axial resolution might be improving as NA increase, the ability of a system to resolve more depth information decreases.

CHAPTER 3

Spatiotemporal Advancements in Microscopy

3.1 Reasoning

With the advent of Fluorescence Microscopy, a flurry of unforeseen levels of utility came into play from the tool. Finally, with the introduction of GFP, living cell dynamic imaging took life. Since then, a large portion of the development in light microscopy imaging has been in speeding up the tool to image faster and faster dynamics. For example, complex organisms like *Danio rerio*, Zebrafish, a vertebrate animal, has neural dynamic processes on the order of 1-10s of milliseconds, Eimon et al. (2018) [23]. For cardiovascular processes, like heart rate, those can beat at 120–180 bpm, Sampurna et Al. (2018)[24]. Currently, there are a lot of tools that can image at these speeds with relative ease, however, the caveat is that most methods can only do so in 2D fields of view only. Nevertheless, when imaging only in 2D, a great deal of information is lost because these are inherently 3D structures that are being studied. For that reason, people have been trying to increase not only spatial resolution of microscopes, but also temporal resolution in 3D.

3.2 Confocal Microscopy

When light illuminates the entire field without, this type of microscopy is known as *Widefield.* System wise, this is the most convenient method illuminate a sample due to its simplicity as shown in Figure 2.3. However, this type of illumination does come with its own drawbacks. Due to the decrease depth of field produced by large NA systems, most of the light that is being captured is out of focus light and therefore contaminates the light would otherwise follow resolution limit expressions.

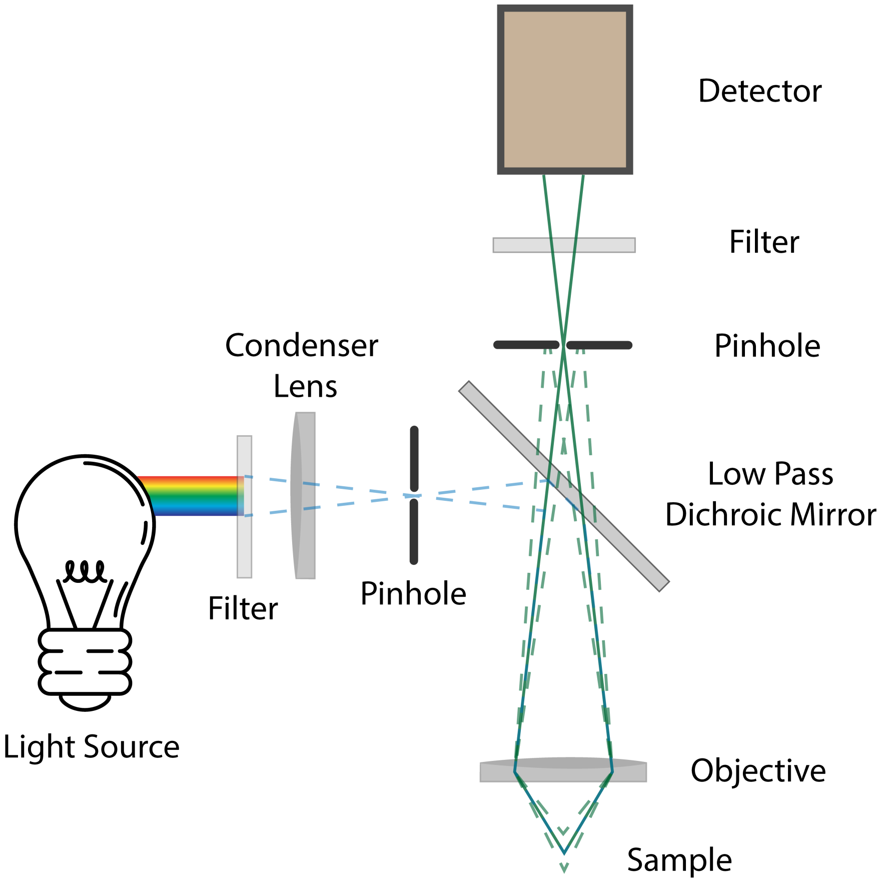
Detector
Filter
Pinhole
Condenser Lens
Low Pass Dichroic Mirror
Filter
Pinhole
Light Source
Objective
Sample

Figure 3.1: *Point Confocal Microscopy.* Invented by Marvin Minsky, in 1957, the point confocal microscope clarified a fuzzy Widefield traditional method by rejecting out of focus light.

In 1957, Marvin Minsky, came up with an ingenious method by which to remove this contaminating, out of focus light [25]. He noted, that at the imaging plane, while most of the light was was out of focus, the image was still being formed at or near its theoretical limit. One could reject the out of focus light simply by placing a pinhole in the formed image location equivalent to the object illuminated location. Due to the point confocal nature of the design, new innovative systems have since invented that allow for the image of larger areas by either translation of the sample on a motorized stage or by deviating the light source with motorized deflection mirrors which in most cases now is a coherent light source (laser). Eventually, these were able to produce up to a few images per second. However, they remained bandwidth limited by the point scanning nature of the system.

It can been from the Airy disk formation figure that most of the intensity is contained within the radius of the first dark ring. In fact, if one were to model that first lobe as a Gaussian distribution, one can see that at,

$$(ka\omega)_{cutoff} = \frac{1.220\pi}{2}, \tag{3.1}$$

$$\omega_{confocal} = \frac{0.610}{2}\frac{\lambda}{a} = 0.310\frac{\lambda}{a}. \tag{3.2}$$

half the distance to the first dark ring, approximately 70% of the information is retained. Here is where by placing a pinhole increases the overall resolution of the system. Not only does the pinhole remove widely distributed the outer rings of the Airy disk, but also decreases the overall width of the central lobe, resulting in a increase of lateral resolution by a factor of 2. See Figure 3.2.

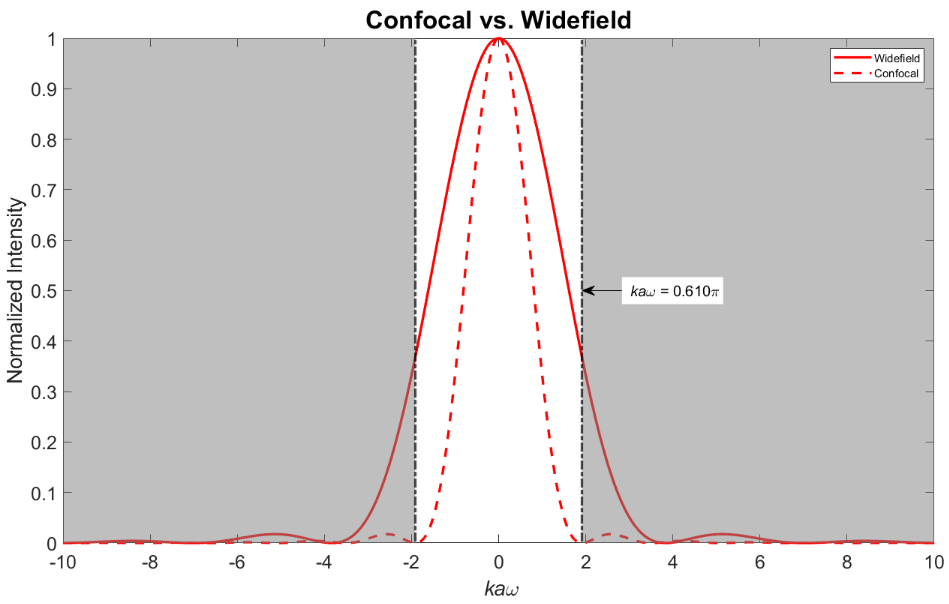

Figure 3.2: *Widefield vs. Confocal Comparison.* By placing a pinhole at approximately half the distance to the first dark lobe, the overall lateral resolution of the system can be increase by a factor of 2 while retaining nearly of the input intensity. The solid line indicates what a widefield system would see. The dashed red line indicates the compression of the first lobe down by a factor of 2 after applying a confocal pinhole.

3.2.1 Spinning Disk Confocal Microscopy

To increase the speed, David Egger and Mojmír Petráň, shortly after the invention of the point confocal, in 1967 took and old device called the Nipkow disk and reapplied to the recently invent point confocal technique [26]. This move parallelized the point-by-point process such that images capture increase several order of magnitude. Currently, state-of-the-art systems, like the Yokogawa Spinning Disk Confocal module (CSU-X1)[27] can routinely take images up to 2000 frames per second, attached to the appropriate sensor.

3.2.2 Line-Scanning Confocal Microscopy

Another method to parallel process the acquisition of data that has confocality in mind is Line-Scanning Confocal Microscopy (LSCM) [28, 29]. Instead of acquiring data on a point-by-point basis, LSCM utilizes a standard feature in modern scientific Complementary Metal–Oxide–Semiconductor (sCMOS) cameras, like the Hamamatsu Flash 4.0 v2 (Hamamatsu Photonics K.K., Hamamatsu City, Japan), which can activate only a subset of pixels and not allowing the adjacent pixel rows to collect photons. Each pixel column (times active pixels) is routed to its own Analog-to-Digital (A/D) converter. This has the same effect that a pinhole would have, but only in one dimension. Using a scanning galvanometer, a laser line can be synchronized with the rolling shutter. See Figure 3.3.

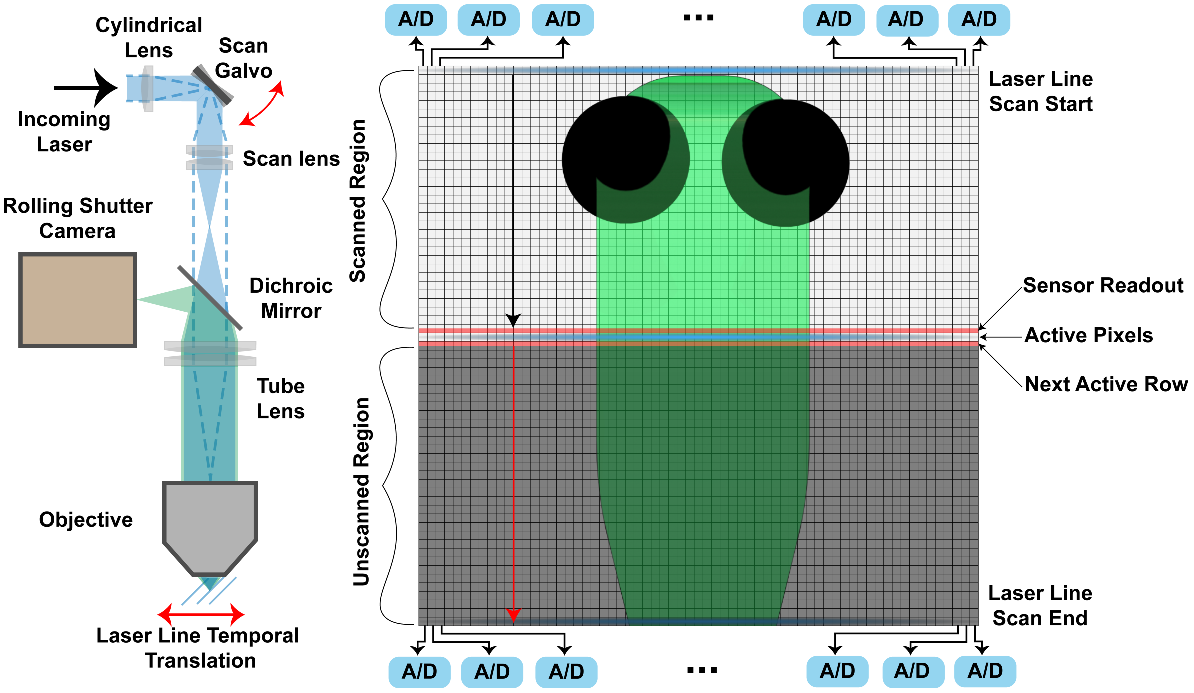
Cylindrical Lens
Scan Galvo
Incoming Laser
Scan lens
Rolling Shutter Camera
Dichroic Mirror
Tube Lens
Objective
Laser Line Temporal Translation
A/D
...
Scanned Region
Unscanned Region
Laser Line Scan Start
Sensor Readout
Active Pixels
Next Active Row
Laser Line Scan End

Figure 3.3: *Line-Scanning Confocal Microscopy.* By focusing light down to a line using a cylindrical lens, that scanning of that line can be synchronized with the rolling shutter of modern sCMOS cameras. The net effect is a system that is half widefield and have confocal. In the direction of the shutter, confocality exists whereby the rolling shutter rejects out of focus light, while in the orthogonal direction, widefield is present.

The resulting point spread function (PSF) is a convolution of the point confocal PSF in the X-dimension and a widefield PSF in the Y-dimension, where the PSF is elongated along the direction of the active pixel rows,

$$d_{lateral,x} = 0.310\frac{\lambda}{NA}, \tag{3.3}$$

$$d_{lateral,y} = 0.610\frac{\lambda}{NA}, \tag{3.4}$$

Although the overall PSF has increased in size, the benefits gained can arguably out weigh the negative side effects. Namely, the speed of the system can be increased dramatically. sCMOS cameras, like the Hamamatsu Flash 4.0 v2 have "light-sheet" modes that can acquire full frame images of 2048 pixels × 2048 pixels at 50 FPS. Newer sensors has the capability to capture in this mode with even larger sensor areas at 100 FPS (Hamamatsu Flash Fusion) [30] or even 121 FPS (Hamamatsu Flash Lightning) [31] under its rolling shutter mode. Previously, the bottleneck of confocal systems was the scanning speed by which you could scan and area point by point. By parallel processing the illumination and acquisition in 1 dimension, the entire process was sped up at the cost of some lateral resolution.

3.3 Light-Sheet Microscopy

By illuminating orthogonal to the detection axis, the main issues that plague single objective imaging, namely: phototoxicity, photobleaching and optical out of plane light contamination, to name a few. The first iteration of a light-sheet microscope used a cylindrical lens to create the sheet, which results in approximately a thin widefield section equivalent lateral resolution. Lately, innovative techniques have unfolded so further increase the resolution. Similarly to LSCM, a thin "pencil" like Gaussian beam can be created using a spherical lens and translated along the detection plane using a galvanometer. Ahrens et al. (2013)[2] managed to image Zebrafish in whole at 0.8 Hz using a more sophisticated version using dual detection and illumination objectives, which they named IsoView. With this illumination methodology, a confocal conjugation with the imaging sensors rolling aperture can be used, thereby increasing the resolution in the lateral and axial dimensions. See Figure 3.4.

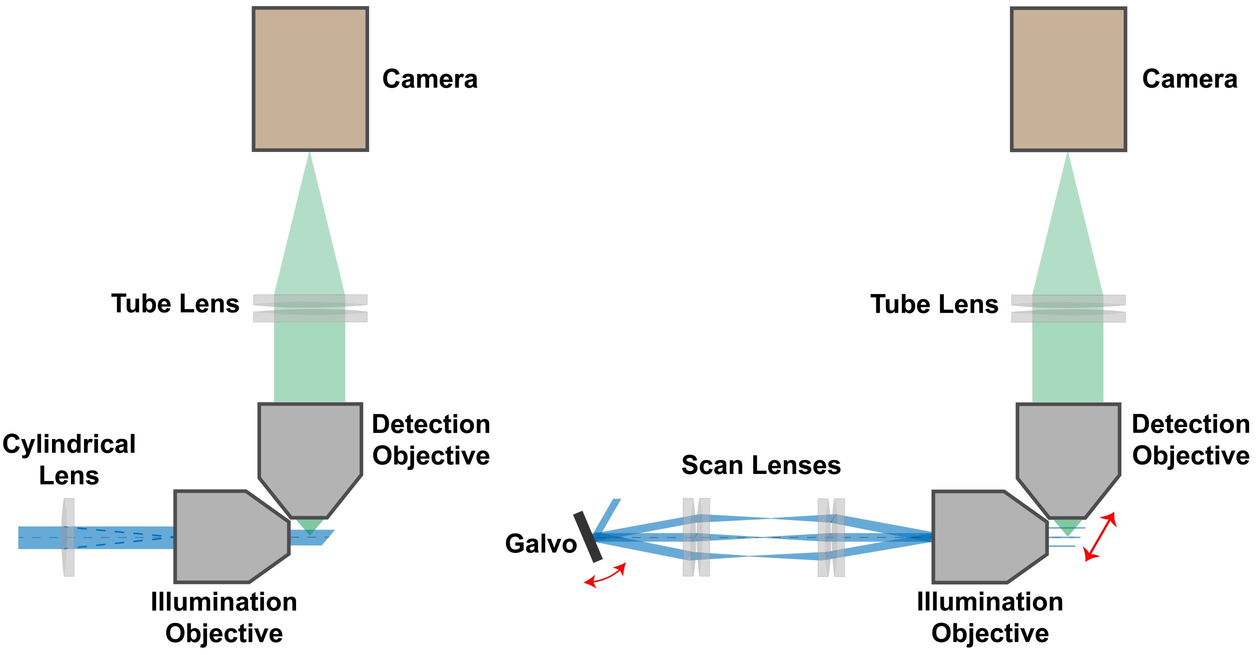
Camera
Tube Lens
Cylindrical Lens
Detection Objective
Illumination Objective
Camera
Tube Lens
Scan Lenses
Galvo
Detection Objective
Illumination Objective

Figure 3.4: *Light Sheet Microscopy.* Conventional light-sheets (*left*) are created using a cylindrical lens to focus the light only in one dimension. To create ”pencil-like” beams, *right* that are instead scanned confocally with the rolling sCMOS sensor, the methodology is to use a regular spherical lens, rather than a cylindrical lens.

Even further, sub diffraction limit beams have been created by implementing Airy beams, Vettenburg et al. (2014)[32], non-diffracting beam profiles like Bessel-Gauss beams and optical lattices of said beams which are formed by conical phase profiles, Betzig (2005) and Chen et al. (2014) [33, 4]. See Figure 3.5. The general purpose for this type of beams is not only their resolution improvements, but also because the beams propagate for longer distances than standard Gaussian beams are the same numerical aperture focusing angle.

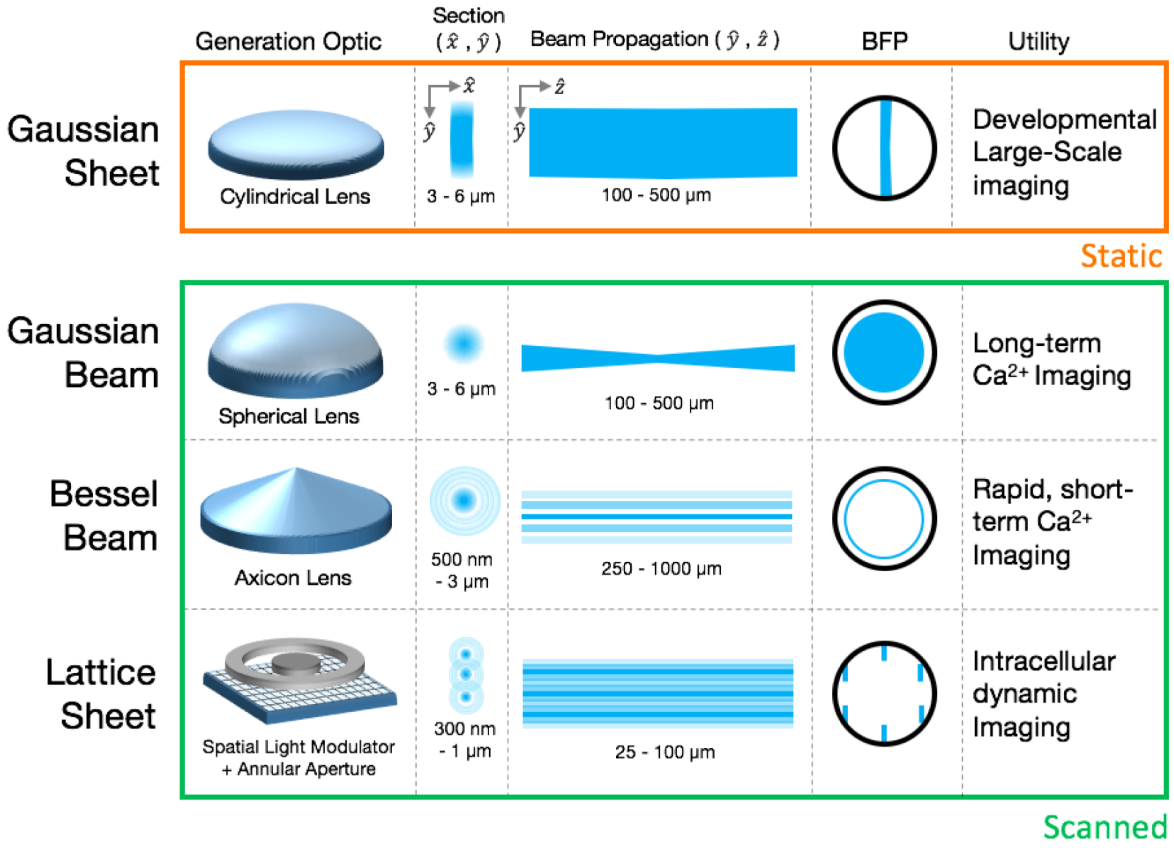
Generation Optic
Section ($\hat{x}$, $\hat{y}$)
Beam Propagation ($\hat{y}$, $\hat{z}$)
BFP
Utility
Gaussian Sheet
Cylindrical Lens
$\hat{x}$
$\hat{y}$
3 - 6 µm
$\hat{z}$
$\hat{y}$
100 - 500 µm
Developmental Large-Scale imaging
Static
Gaussian Beam
Spherical Lens
3 - 6 µm
100 - 500 µm
Long-term Ca^{2+} Imaging
Bessel Beam
Axicon Lens
500 nm - 3 µm
250 - 1000 µm
Rapid, short-term Ca^{2+} Imaging
Lattice Sheet
Spatial Light Modulator + Annular Aperture
300 nm - 1 µm
25 - 100 µm
Intracellular dynamic Imaging
Scanned

Figure 3.5: *Comparison of Light-Sheet Illumination Beams.* The first and standard beam illumination method is created using a cylindrical lens which collapses a gaussin plane wave in one dimension. The typical propagation length is 100-500 μm, however this type of beam does not afford any confocality application to a rolling shutter sCMOS sensor. For confocality, a spherical lens can be used which collapses the beam in both dimensions with the same propagation distance. Non-diffracting beams created by interference, Bessel-Gauss beams, have a much larger propagation distance, 250-1000 μm, compared to same numerical aperture collapsed Gaussian Beams. With the aid of a Spatial Light Modulator (SLM), an array of Bessel beams can be configured to interfere even further by trimming away at each adjacent beams thereby reducing the overall waist of the beams. Courtesy of Blake Madruga, adopted from his Thesis work on Configurable Bessel-Gaussian Sheet Illumination Microscopy[5].

3.4 Scanned Volumetric Imaging

In the previous sections, discussion was focused on 2D imaging by means of widefield, confocal, or light-sheet illumination. However, due to the minuscule depth of field that large numerical aperture objectives provide (on the order of microns), and the inherent need to image in 3D, methods have been developed image make this possible. There are 2 ways by which this can be achieved according the previous research. The first method is to translate the sample such that is moves in and out of the focal plane of the objective. The second method is to move the objective such that the objective's focal plane is translated relative to the sample. See Figure 3.5.

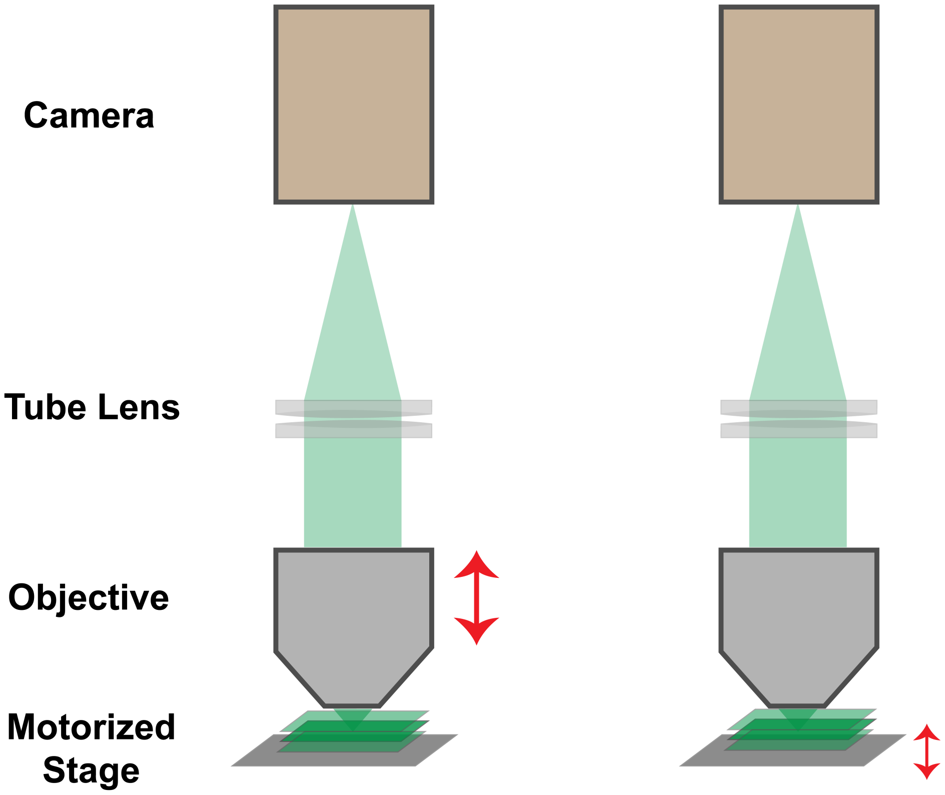

Figure 3.6: *3-Dimensional Scanning.* Two main methods for mechanic depth scanning are the translation of the objective using a piezoelectric actuator (left) and movement of the sample stage using a motorized stage (right).

3.5 Static Volumetric Imaging

Recently, a push has been made to create methods by which the slow translation of an imaging objective or sample can be avoided. The physical translation is an unavoidable requirement due to the highly compressed depth of field associated with high numerical aperture systems. Nevertheless, new methods have surfaced by which to bypass this limitation.

3.5.1 Light Field Microscopy

Standard microscopy methods rely on the capture of incident light onto a sensor. This is usually comprised on 2D information only (stemming from the fact that high NA systems have short depth-of-fields), the rest of the information has or has not already angular converged into an image. For example, an object that is further away from the objective focal plane will have already converged. Conversely with objects closer to the focal plane; they have yet to converge. With the placement of a *microlens array* at the formed image plane, the objects in the objective focal plane that are exactly correlated with the image plane while transmit through only one of the microlenses. However, if they have not yet converged or have already converged will pass through multiple microlens arrays. Now, by placing a detector at the back focal plane (BFP) of the of the microlens array, there will be product of multiple microlens BFP each containing different 2D angular information from the entire volume being imaged. This aforementioned method is known as *Light Field Microscopy* (LFM), Levoy et al. (2005) [34]. Through computational deconvolution, based on the field theory of light, the entire volume can be reconstructed. Limitations of this system lie in the heavy computational resources required to perform this deconvolution, taking somewhere on ”the order of seconds to minutes” for each volume being reconstructed. When dealing with possible dynamic processes that are on the order of milliseconds and recordings are preferred to last up to minutes or even hours, the times required to deconvolve an entire data-set become staggering.

3.5.2 SCAPE Microscopy

With an emphasize being place on a purely optical methodology by which to obtain 3D images, Bouchard et al. (2015)[35], and most recently Voleti et al. (2019)[3] have created a novel system that does not rely on the translation of on object. Rather, it exploits an oblique light sheet illumination and detection scheme in order to capture volumes. Swept confocally-aligned planar excitation (SCAPE) microscopy, see Figure 3.7, is a single object light sheet system that has roots in both LSCM and LSM. By illuminating at an oblique angle, the once convolved depth information, now becomes visible without the need for deconvolution. This oblique light sheet produces fluorescence that is nearly orthogonal in the opposite half of the objective. The signal returns via the same pathway and is descanned by the once scanning galvanometers. Once descanned, the static image is relayed through a pair of objectives where the second objective in the pair looks at the formed image from an oblique angle. The oblique angle is orthogonal angle of tilt that the light sheet was produced. The result is a flat image plane captured by this secondary objective. Overall the system is a very clever way of realigning the image plane such that it is once again flat on the imaging sensor. However, the cost of this is technique is a reduced numerical aperture, approximately 50% reduction in effective NA. Results indicate that when partnered with a HiCAM Fluo intensified CMOS camera (Lambert Technologies, LLC Kissimmee, FL, US), volumes were generated of up to 321 VPS for voxel regions of 57 pixels × 640 pixels × 100 pixels for a maximum bandwidth of 1.2 GPixels/second.

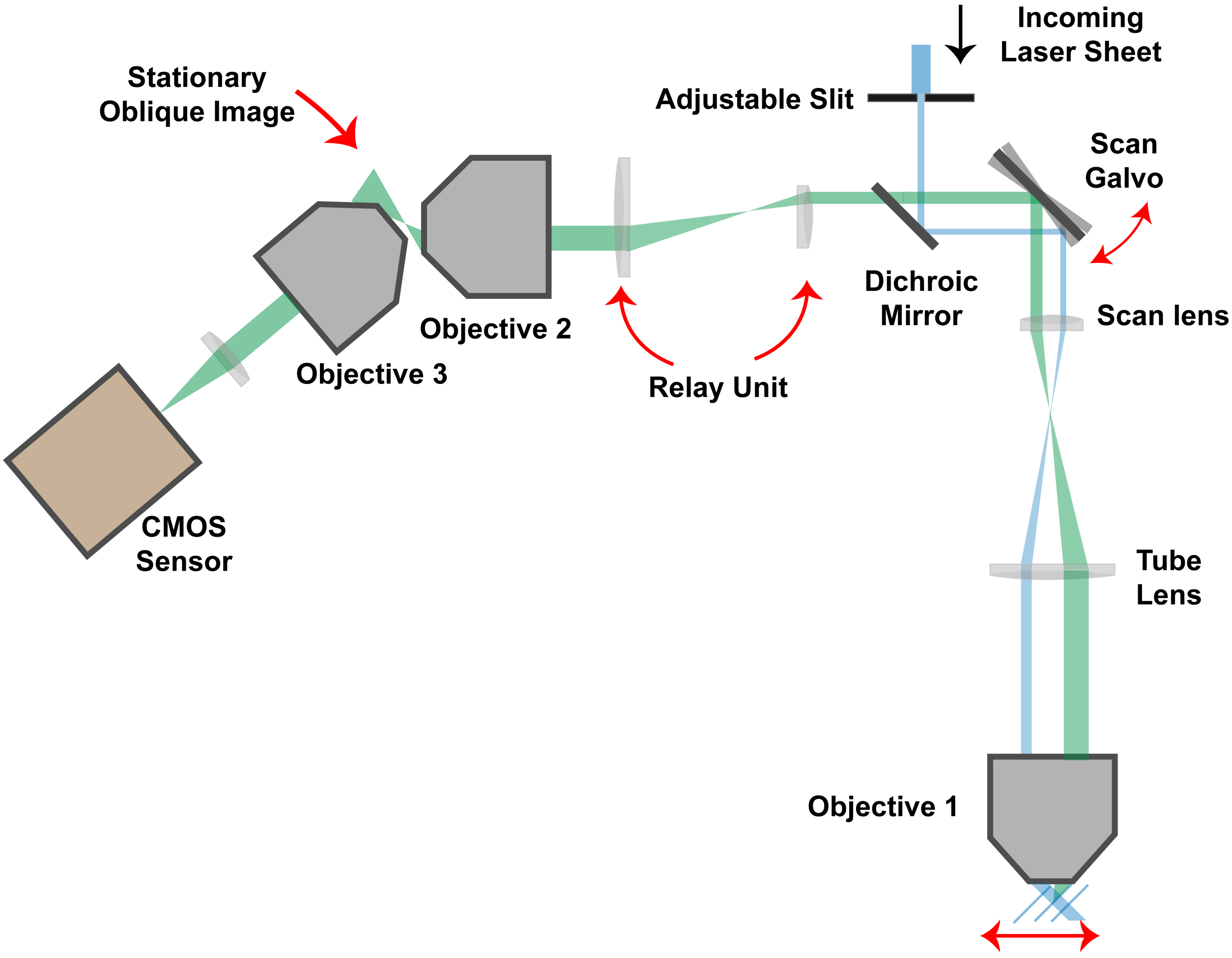
Incoming
Laser Sheet
Stationary
Oblique Image
Adjustable Slit
Scan
Galvo
Dichroic
Mirror
Scan lens
Objective 2
Objective 3
Relay Unit
CMOS
Sensor
Tube
Lens
Objective 1

Figure 3.7: *SCAPE Microscopy.* With a single objective, SCAPE microscopy achieves depth resolved images. To do so, an oblique illumination sheet is implemented. On the detection axis, only the orthogonal directional fluorescence is utilized. After descanning, the descanned plane, is relayed to a secondary objective whereby utilizing a tertiary, the image plane is mapped onto a flat image plane and onto an imaging sensor.

3.5.3 Deep-Z Microscopy

Due to the astounding capabilities of computational neural networks to understand 2D images, researchers have applied the networks to microscopy. By using standard microscopy modalities (*i.e.* widefield, confocal), Wu et al. (2019)[36], of The Ozcan Research Group at UCLA, were able to reconstruct out of focus information up to ±10 μm from the initial focal plane. This knew technique breaks an important boundary in 2D $\rightarrow$ 3D microscopy, where the computational reconstruction limitation of time can be bypassed, like that required in LFM deconvolution. In Figure 3.7, Deep-Z is detailed in its methodology. A sample image set (training data set) at various foci of the point spread function are fed into a digital propagation matrix (DPM), where it learns to classify a multitude of information cues of those images. Once the network is trained, a single input frame at the focal plane can be feed and the digital propagation network, or Deep-Z, refocuses once out of focus information. Although the training of the network might take a non-trivial amount of time, the training is a one time event and can be used for any future images from that microscope.

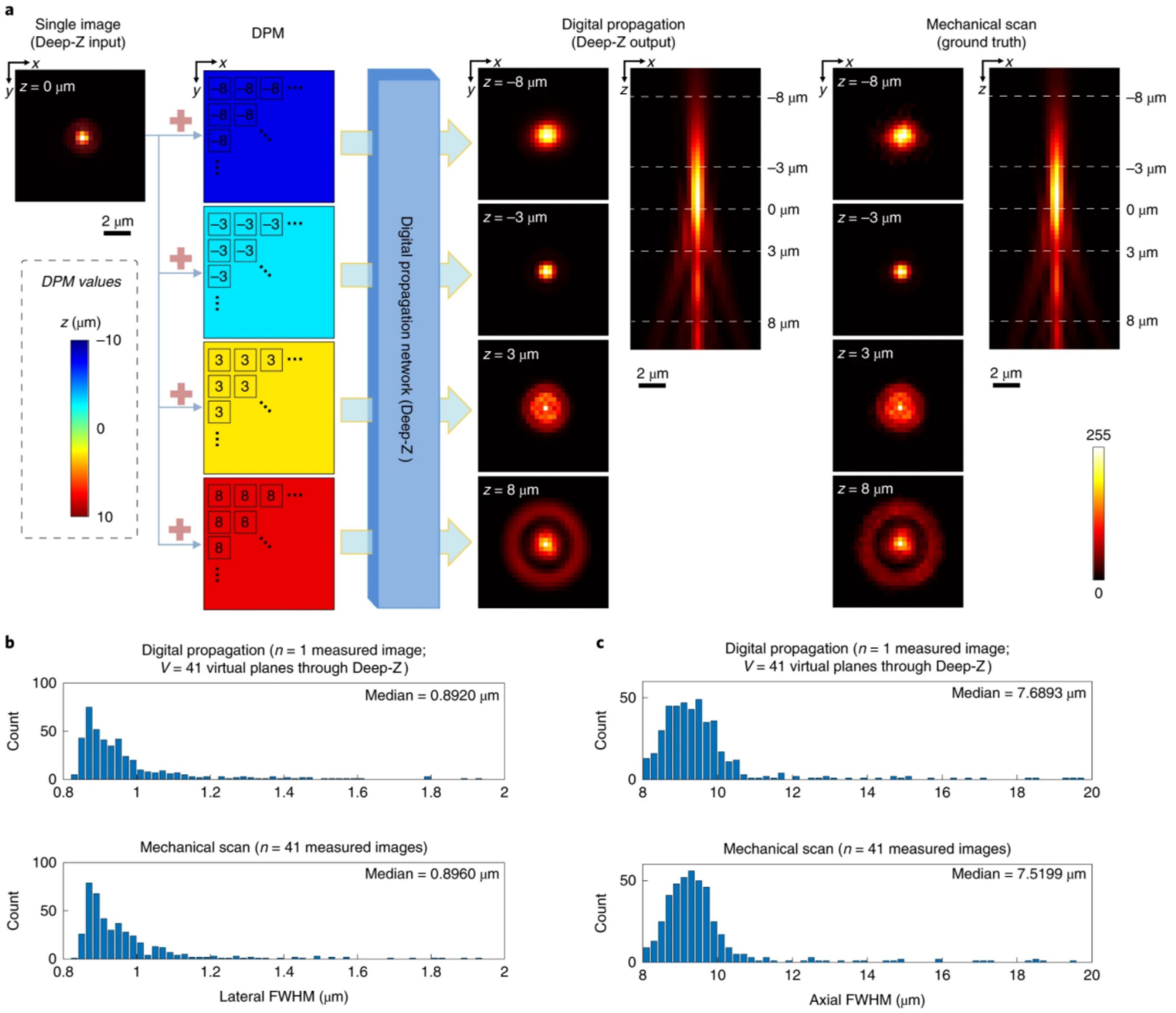

Figure 3.8: *Deep-Z Microscopy.* Single plane images are feed into a trained neural network, where the are refocused up to distance of $\pm 10\mu$m. For conformation, the Deep-Z generated refocused images are compared to the mechanical translations focused images for a fluorescent bead (a). (b) is distribution of the FWHM of 300 nm fluorescent beads in the lateral dimension for both Deep-Z propagation and mechanical objective translation. Similarly for (c), the axial dimension FWHM are measure. In both cases, it is seen that the Deep-Z propagation matches very well with the mechanical translation.

3.5.4 Transverse-Sheet Illumination Microscopy

Transverse-Sheet Illumination Microscopy (TranSIM) is a new microscopy method is presented that utilizes previous work, namely LSCM illumination and detection methodologies, and also novel methods to attack the problem of fast 3D microscopy. By parallel processing the scanning method of LSCM, much like Spinning Disk Confocal parallel processed the illumination and detection of its Point Confocal predecessor, TranSIM is able to speed up acquisition by several orders of magnitude. In addition, the depth refocusing methodology, removes the slow mechanical translation seen in some previous systems, which tended to be a bottleneck when it came to volumetric imaging. To do achieve such speeds, TranSIM takes the light sheet produced by cylindrical lens and multiplexes it such that is has a lateral and axial separation, therefore, the light that is no longer convolved in its propagation. This allows for a purely optical method by which to detect the separate image planes being illumination. Upon return though the scanning optics, the image planes are then injected into a cyclic focal plane readjustment apparatus that maps the multiplexed images into several image sensors. Overall, in this version, the system was optimized to image 9 separate image planes at 200 Hz, for a total bandwidth of 0.56 GPixels/second, with research standard cameras like the Hamamatsu Flash 4.0 v2. Moreover, the speed can be improved by instead utilizing newer, faster sensors like the Hamamatsu ORCA Fusion and ORCA Flash Lightning, which have pixel rates of 0.53 GPixels/second and 1.45 GPixels/second, respectively. This would bring the total bandwidth of the current TranSIM configuration of 3 cameras to a theoretical maximum of 1.59 GPixels/second, for a Fusion system, and 4.35 GPixels/second for a Flash Lightning system. In addition, the novelty of the cyclic focal plane rearrangement techniques allows for the addition or subtraction of cameras, depending on the requirement and it does so while maintaining near diffraction limit resolution. With this illumination and detection method, volumes of up to 200 VPS were capture of the *Caenorhabditis elegans* and *Danio rerio*. In the case of *Danio rerio*, dynamic processes that are seen in 3D. In the following chapter, a detailed view of how TranSIM operates is discussed.

3.6 Volumetric Rates and Bandwidth

Below in Table 3.1, a comparison of the latest microscope technology is presented to gain a broader understating of the speeds that are currently available to conduct scientific inquiries. It is evident that the domains of time, volume, and resolution, are interrelated by a common principle, and that is *bandwidth*, grey column. Furthermore, although bandwidth is a great indicator of the imaging speed of a system, the lack of *sensor-to-sensor* comparison renders the question more complex. Given that some systems do utilize sensors that have an intrinsically faster bandwidth, the overall bandwidth is bound to be larger. For example, when comparing a Hamamatsu Flash 4.0 v2 to a HiCam Fluo Image Sensor CMOS camera, the repetition rate of the digitizers are completely different. Succinctly, the Flash 4.0 v2 has a maximum frame rate of 50 FPS (under light-sheet mode) for a pixel area of 2048×2048 pixels^2. Conversely, the HiCam Fluo has a frame rate of 1000 FPS at 1280×1024 pixels^2. This results in a maximum bandwidth of 0.21 GPixels/s (Flash 4.0 v2) versus 1.31 GPixels/s (HiCam Fluo). Nevertheless, if paired with identical sensors, the system that utilizes the most overall sensors is the system with the theoretical maximum bandwidth. Having been said, total volume imaged per unit time is another valid form of comparison, given that much of the research is put forth in order to cover more volume, faster.

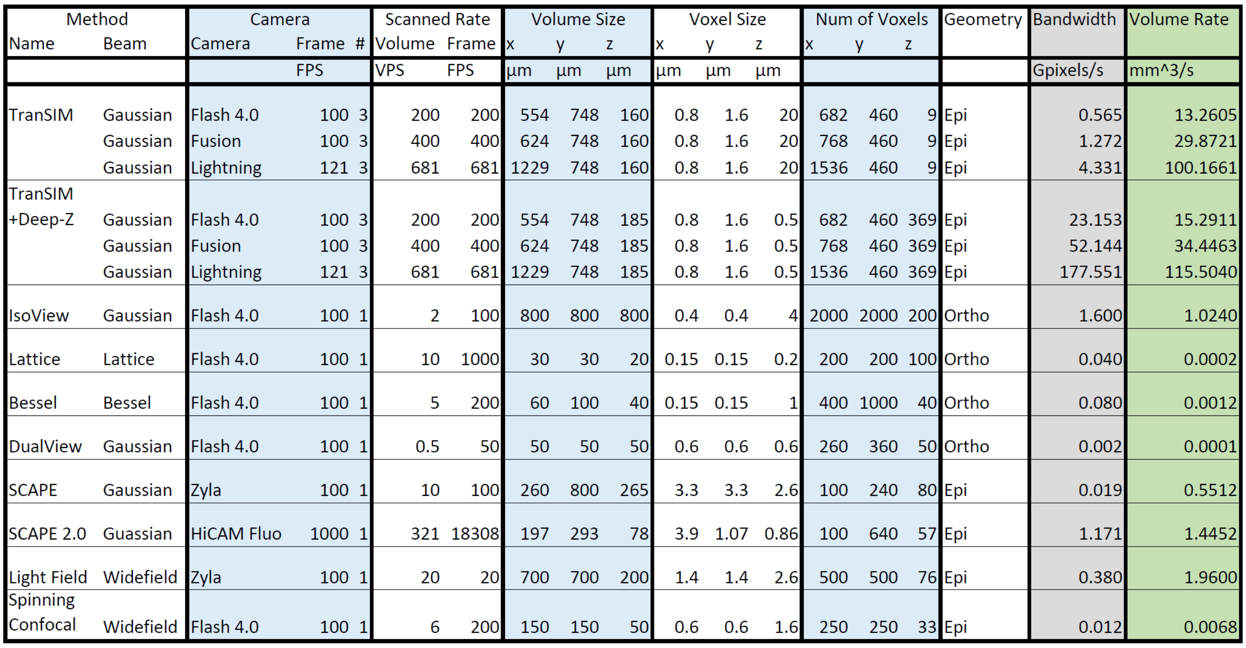

Method		Camera			Scanned Rate		Volume Size			Voxel Size			Num of Voxels			Geometry	Bandwidth	Volume Rate
Name	Beam	Camera	Frame	#	Volume	Frame	x	y	z	x	y	z	x	y	z			
			FPS		VPS	FPS	µm	µm	µm	µm	µm	µm					Gpixels/s	mm^3/s
TranSIM	Gaussian	Flash 4.0	100	3	200	200	554	748	160	0.8	1.6	20	682	460	9	Epi	0.565	13.2605
	Gaussian	Fusion	100	3	400	400	624	748	160	0.8	1.6	20	768	460	9	Epi	1.272	29.8721
	Gaussian	Lightning	121	3	681	681	1229	748	160	0.8	1.6	20	1536	460	9	Epi	4.331	100.1661
TranSIM +Deep-Z	Gaussian	Flash 4.0	100	3	200	200	554	748	185	0.8	1.6	0.5	682	460	369	Epi	23.153	15.2911
	Gaussian	Fusion	100	3	400	400	624	748	185	0.8	1.6	0.5	768	460	369	Epi	52.144	34.4463
	Gaussian	Lightning	121	3	681	681	1229	748	185	0.8	1.6	0.5	1536	460	369	Epi	177.551	115.5040
IsoView	Gaussian	Flash 4.0	100	1	2	100	800	800	800	0.4	0.4	4	2000	2000	200	Ortho	1.600	1.0240
Lattice	Lattice	Flash 4.0	100	1	10	1000	30	30	20	0.15	0.15	0.2	200	200	100	Ortho	0.040	0.0002
Bessel	Bessel	Flash 4.0	100	1	5	200	60	100	40	0.15	0.15	1	400	1000	40	Ortho	0.080	0.0012
DualView	Gaussian	Flash 4.0	100	1	0.5	50	50	50	50	0.6	0.6	0.6	260	360	50	Ortho	0.002	0.0001
SCAPE	Gaussian	Zyla	100	1	10	100	260	800	265	3.3	3.3	2.6	100	240	80	Epi	0.019	0.5512
SCAPE 2.0	Guassian	HiCAM Fluo	1000	1	321	18308	197	293	78	3.9	1.07	0.86	100	640	57	Epi	1.171	1.4452
Light Field	Widefield	Zyla	100	1	20	20	700	700	200	1.4	1.4	2.6	500	500	76	Epi	0.380	1.9600
Spinning Confocal	Widefield	Flash 4.0	100	1	6	200	150	150	50	0.6	0.6	1.6	250	250	33	Epi	0.012	0.0068

Table 3.1: *Microscope Comparison.* Entire parameter space of various microscopes are listed in the area of volumetric scanning. Major research developments in microscopy have taken place in order to increase the speed are which they can image volumes. Although their suitable application domains vary wildly from system to system, the overarching connection is *bandwidth.* In the *grey* column, the total bandwidth of the system is shown in units of GigaPixels/s. Moreover, the *green* column by-passes any sensor non-equivalences, and instead focuses on the total volumetric imaging field imaging rate that is achieved in mm^3/s, or volume size times the volume rate, of each system. Also shown, are proposed versions of *Transverse-Sheet Illumination Microscopy*, in addition to its first proof-of-concept. These future additions aim to explore the possibility of increased throughput of the system, limited only by the bandwidth of the current imaging sensors. Courtesy of Dr. Arisaka, adopted microscope comparison in NIH R21 Proposal to include experimental results of TranSIM[1].

CHAPTER 4

Methods

4.1 Optical Design

TranSIM relies on a multiplexed imaging scheme that is laterally and axially separated and scanned across the imaging field. The result is a system that can be demixed by carefully placing deflecting knife-edge mirror. In Figure 4.1, an optical schematic of the system is displayed in its entirety. In subsections 4.1.1 and 4.1.2, the way the illumination and detection profiles, respectively, are created are discussed in detail. For this proof-of-concept, a 3 detection camera detection system was selected to maximize the number of image plane real-estate that was mapped onto the sensors. Overall, each plane was mapped to 682 pixels × 460 pixels, for a total of 3 planes per camera, thereby spanning the entire sensors and "light-sheet" mode was applied to produce a confocal system and reject out of focus light.

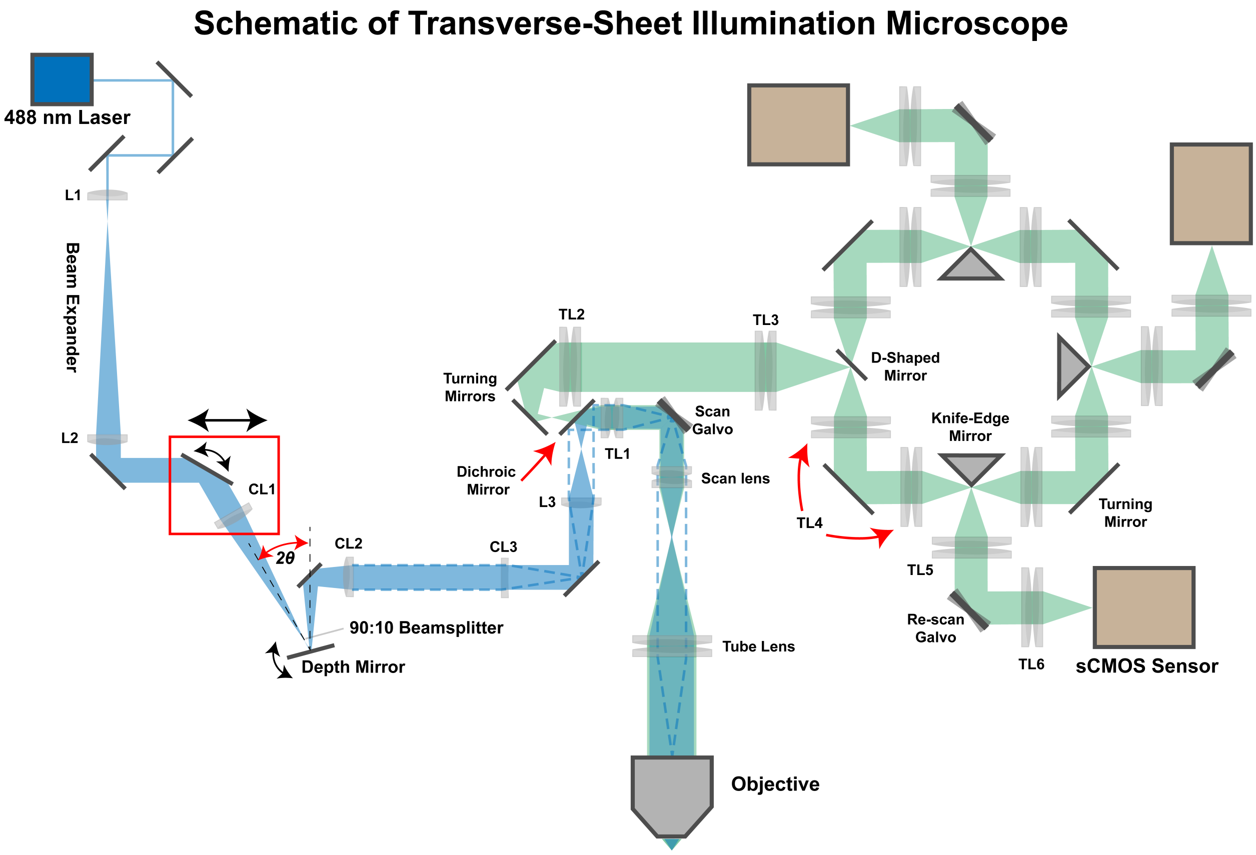
Schematic of Transverse-Sheet Illumination Microscope
488 nm Laser
L1
Beam Expander
L2
CL1
2θ
CL2
CL3
90:10 Beamsplitter
Depth Mirror
Dichroic Mirror
L3
Turning Mirrors
TL2
TL1
Scan Galvo
Scan lens
TL3
Tube Lens
Objective
D-Shaped Mirror
Knife-Edge Mirror
TL4
Turning Mirror
TL5
Re-scan Galvo
TL6
sCMOS Sensor

Figure 4.1: *Schematic of Transverse-Sheet Illumination Microscopy.*

Beginning with the excitation laser, 100 mW Coherent Sapphire 488 nm (Coherent Inc., Santa Clara, CA, United States), the beam is expanded 10X using a telescope beam expander (L1 and L2 spherical doublets, 25 mm and 250 mm, respectively) from its $1/e^2$ gaussian profile of approximately 1 mm to $10/e^2$, resulting in a 10 mm illumination beam. Using an adjustable deflection mirror, the beam is condensed down to a laser line using a cylindrical lens (CL1, 200 mm) and diverted to a depth reflection mirror. The depth reflection mirror reflects the laser line onto a 90:10 Reflection:Transmission beamsplitter. Upon reflection, the beam divergence creates an axial separation added to each subsequent reflected beam. In addition, the angle of incidence adds a lateral translation to each multiplexed beam. After reflection, the multiplexed beams are relayed using a pair of cylindrical lenses (CL2 and CL3, 200 mm and 100 mm, respectively). CL3, is chosen to expand the beam according to the how wide of an imaging field. Spherical lens L3 (100 mm) determines the NA of the excitation. Using a long pass dichroic mirror, the beam is diverted to a telecentric lens formed using a pair of spherical doublet lenses (200 mm) onto a scanning galvo. Similarly, the galvanometer scans onto a telecentric scan lens with effective focal length (EFL) of 100 mm. The 200 mm telecentric tube lens is created using a pair of 400 mm spherical doublets. The excitation beam illuminates the sample and the fluorescence returns via the same pathway, where it is de-scanned by the scanning galvo. Telecentric lenses TL2 and TL3 (formed using 400 mm and 300 mm doublet pairs) are chosen as the primary magnification lens pairs. Focusing the image field onto a D-shaped mirror, the fluorescence is injected into the imaging cycle that will consequently separate and remap the image planes onto the sensors. To relay the image field, identical telecentric lenses (TL4, formed using a pair of 200 mm spherical doublets) and a turning mirror are configured into a 90 degree turn. The knife-edge mirror is then moved into proximity of the first imaging plane it is diverted into the imaging sensor pathway. Before reaching the sensor, the image plane is adjusted for magnification using telecentric lenses (TL5 and TL6, 100 mm EFL, respectively) and rescanned using a galvo temporally synchronized with the primary scanning galvo. Additional planes move onto the next knife-edge mirror where the adjacent image plane is diverted to the second sCMOS sensor. Likewise, for the third image plane. After the first cycle is nearly complete, the remaining image field is adjusted using the last telecentric unit, such that it is depth refocused to be on top of the first image plane and laterally adjacent. The cycle continues and each camera images the appropriate number of planes (3 planes per camera in this configuration)

4.1.1 Beam Multiplexing

To create the illumination beams, a simple reverberation technique was employed by placing two parallel mirrors, one with a transmission coefficient of 0.1. This method creates an ad infinitum sequence of multiplexed beams that have 10% of the previous reflection,

$$I_n = 0.1 * I_0 * 0.9^{(n-1)}, \tag{4.1}$$

where, I_{n}, is the n^{th} multiplexed beam, I_0, is the initial incoming laser beam intensity. Additionally, the lateral and axial separations are governed by the following geometric equations,

$$z = \frac{d}{cos(\theta)}, \tag{4.2}$$

$$y = z * tan(\theta). \tag{4.3}$$

Something to consider when it comes to illuminating the sample because the method produces a non equal illumination scheme that has highest intensity at the top of the sample. However, in order to remedy an unequal illumination, a variable density filter can be applied to the beams, but an adequate laser source should be considered for the intensity losses.

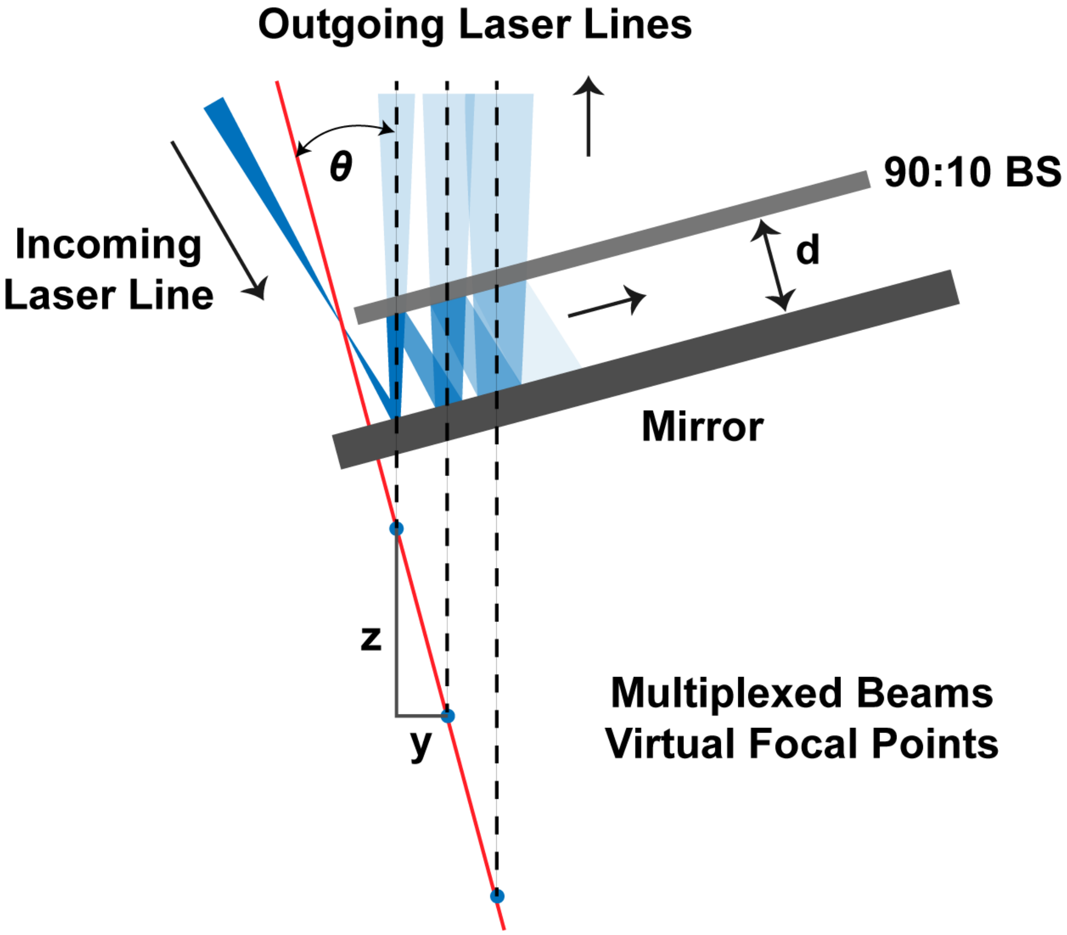
Outgoing Laser Lines
θ
90:10 BS
Incoming
Laser Line
d
Mirror
z
y
Multiplexed Beams
Virtual Focal Points

Figure 4.2: *Laser Line Beam Multiplexing.* To create a 9 imaging planes with laser line focus, a single laser line created using a cylindrical lens is reflected an angle, θ, to the normal of depth refection mirror. The light then travels to a 90:10 broadband beamsplitter (BS), where 90% of the light is reflect back onto the mirror at angle angle θ and 10% is transmitted. The process continues ad infinitum; for the purposes of TranSIM, 9 useful beams are ultilized. Each reflection beam created has 10% of the previous reflection, therefore, the intensities of the beams decay by power law. To increase the later separation y, the angle θ can be adjusted. To increase the depth separation, the distance, d can be increase. The only requirement is that the beamsplitter and depth reflection mirrors maintain a parallel geometry, otherwise the beams will begin diverge.

4.1.2 Plane Separation and Focal Plane Readjustment

Following the descanned (static) image field into the cycle, the image planes are focused where they have axial and lateral separations. This allows for a knife-edge mirror to be introduced and divert the one of the image planes on to the sensor detection path where it will be re-scanned before reaching the sensor. See Figure 4.3. The remaining image planes continue forward where they are relayed using a pair of telecentric lenses and right angle turning mirror onto the second stage. The same principle applies and the second single image plane is deflected onto the second sensor. This continues one more time for the third stage.

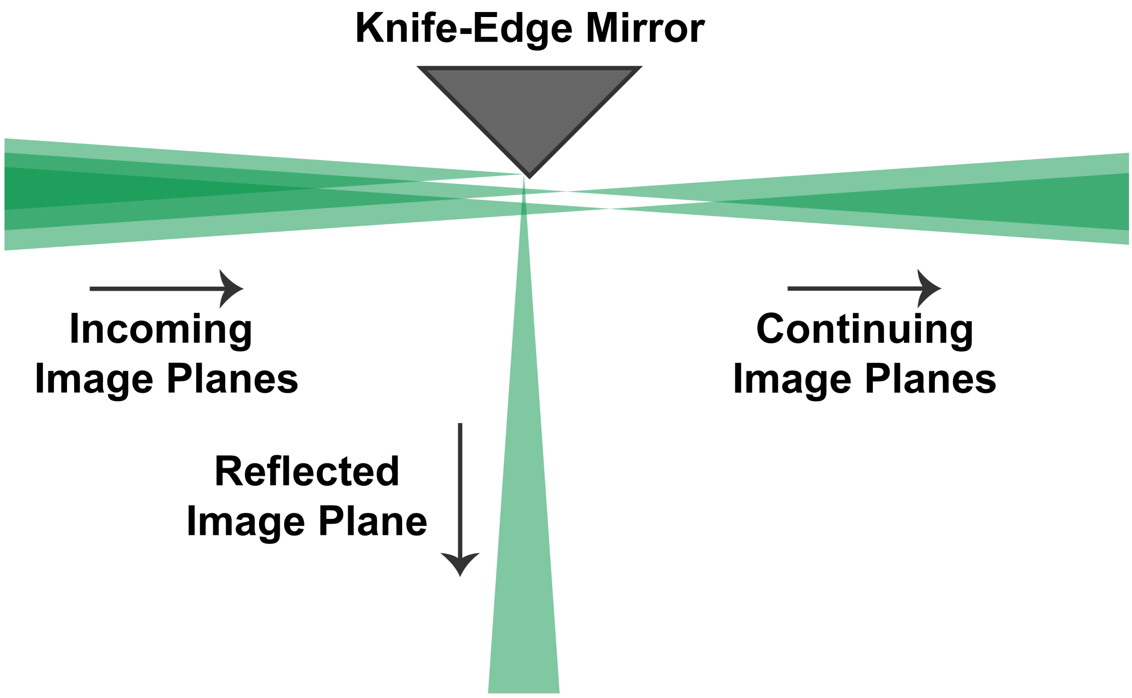

Figure 4.3: *Plane Separation.* After injection into the cyclic apparatus, the beams now undergo separation. To separate the planes, the beams are focused down to an image where they retain have axial and lateral separation. Using a knife-edge mirror, a single image plane can be reflected into the imaging sensor and the remaining planes are allowed to continue undisturbed.

After completing one cycle, the last relay lens unit does the job of readjusting the new focal plane location and lateral translation of the image plane such that it lies adjacent to the previous cycle. See Figure 4.4. To do so, the last relay unit can be moved in tandem to laterally translate the image plane such that, for example, image plane 1 and 4 lie on the same location along the y-axis. However, this would place is right behind the D-Shaped mirror which was used to insert the planes into the cycle. To cure this problem, similarly to the y-axis translation, the entire relay unit can be translated in tandem in the x-dimension, this will translate the image plane to lie adjacent to the previous image plane. Lastly, to refocus the image plane such that it is congruent with the previous cycle, the last telecentric lens is translated forward, pushing the focal plane location with it. The cycle repeats.

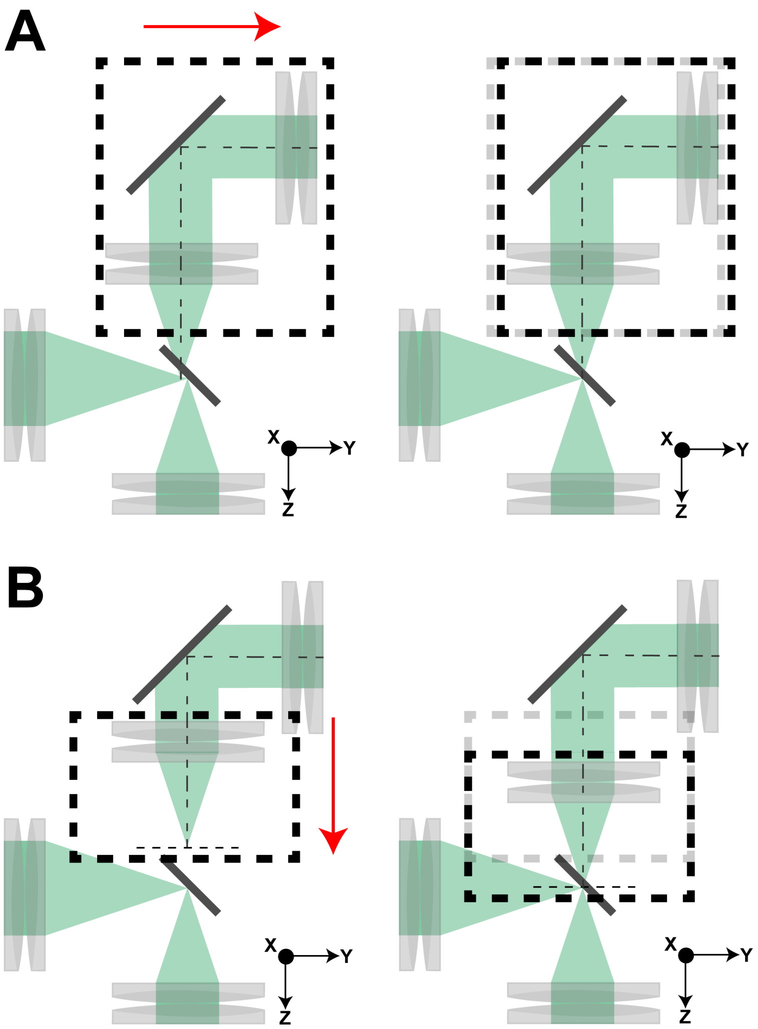

Figure 4.4: *End of Cycle Readjustment Process.* After the first cycle, image field would return to the same location as when it started the cycle. Using the last telecentric relay unit, the planes can be refocused axially and readjusted laterally to remap the adjacently the previous cycle. (A) shows how to laterally translate (in Y-dimension) by taking the telecentric unit and moving is uniformly until the image field returns to a centered position as if the first of the remaining image planes were the first true image plane. Similarly, to move offset in the X-dimension, such that the planes pass underneath the D-shaped mirror, the telecentric relay unit it moved uniformly until the there is enough clearance. (B) For depth, only the last telecentric lens is adjusted such that the image planes are focused to overlap the planes the planes of the previous cycle.

4.2 Data Acquisition and Control

Hardware control and synchronization was conducted on a custom work station based on a Socket TR4 AMD 1950X Threadripper. Each camera was linked via its own FireBird Camera Link Frame Grabbers (1xCLD-2PE8) (Active Silicon Ltd., Pinewood Mews, United Kingdom) connector and routed to separate Samsung 970 PRO NVMe SSDs (Samsung Group, Seoul, South Korea) for data storage and bottleneck avoidance. Control software was custom written in LabVIEW (National Instruments Corporation, Austin, TX, USA) to operate all three cameras simultaneously using the Hamamatsu DCAM-API drivers. Custom waveforms were created in a Matlab script module inside LabVIEW and written to NI PCIe-6363 I/O device (National Instruments Corporation, Austin, TX, USA), which synchronized all the hardware with its on-board clock at 1 GSamples/s. See Figure 4.7. To reduce, galvanometer backlash, the waveform was filtered of high frequency components. See Figure 4.6.

4.2.1 Synchronization Waveforms

Synchronization waveforms comprise of 3 total waveforms; 1 camera galvo, 1 scanning galvo, and 1 camera trigger signal. Sawtooth waveform has a 90% linear travel region that is synchronized with the light-sheet read mode of 3 Hamamatsu ORCA Flash 4.0 v2's. See Figure 4.5 and 4.6. The line-rate was set to maximum with a line interval of 9.7444 μs. The active pixel region was adjusted to fit the FWHM of the laser line, which with an effective magnification of 8X, using the Nikon Plan Fluorite 16X 0.8 NA objective and 6.5 μm pixel pitch, is 2 pixels. For a the Nikon 40X 0.8 NA objective, the active pixel area was set to 3 pixels. Additionally, the scanning galvo amplitude could be altered to fit more or less area onto the same 682 pixel × 460 pixel region. In figure 4.5, the dashed boundaries determine the effective magnification factor (along the Y-dimension only) that can be pragmatically implemented on TranSIM and is,

$$M_{Tot,eff} = M_{0,eff} * (\frac{A_{Cam}}{A_{Scan}}). \tag{4.4}$$

where, $M_{\mathit{eff},Tot}$, is the total effective magnification, A_{Cam}, is the camera galvo amplitude, A_{Scan}, is the sample scanning galvo amplitude, and $M_{\mathit{eff},0}$, is the effective magnification determined by the optics. In essence, much like in point scanning systems, the effective magnification is determined by the amplitude of the scanning waveforms. A similar argument is said for TranSIM, however, the scanning waveforms only have an effect in a singular dimension, the y-dimension. For example, if the sample scanning amplitude of the galvanometer is increased by a factor of 2, then the effective magnification is inversely proportional, resulting in a factor of 2 reduction in magnification.

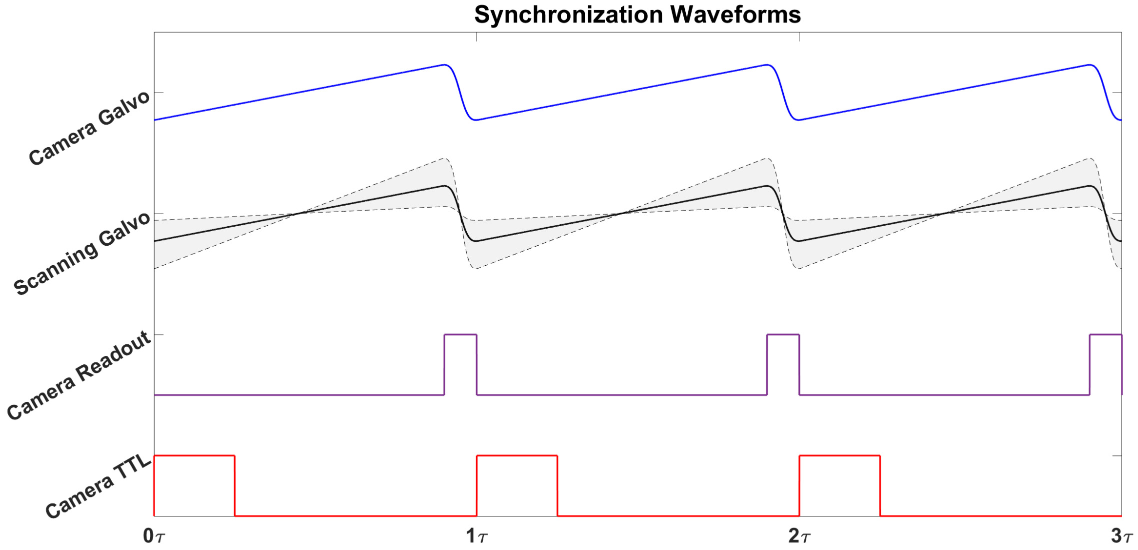

Figure 4.5: *Synchronization Waveforms.* Three Hamamatsu Flash 4.0 V2s are synchronized by a parallel TTL signal. The field scanning galvanometer has a smoothed out sawtooth waveform. On the reset travel time, the camera's undergo readout. The image field is de-scanned due to the backward propagation through the detection arm onto the scanning galvo. After plane rearrangement, the image planes are rescanning using the camera located galvanometers. TranSIM allows for 1-dimensional spatiotemporal compression (similar to point confocal systems whereby the scan range determines the magnification) by expanding or contracting the amplitude of the scanning galvo while maintaining the camera galvo-camera line-scanning matched. Lower and upper boundaries denoted by dashed lines correspond to 0.25X and 2X magnification, respectively, for demonstrative purposes.

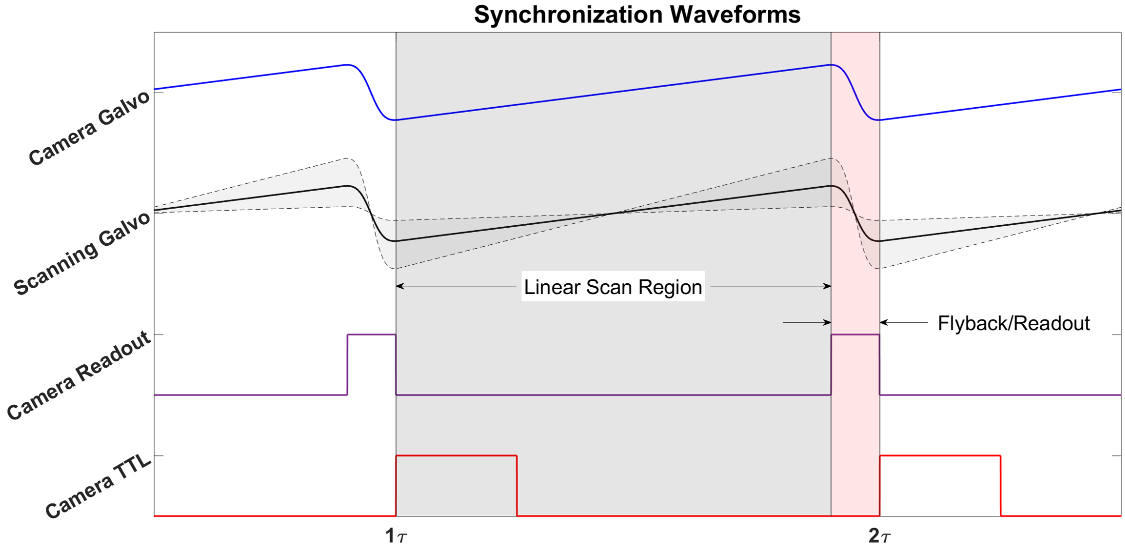

Figure 4.6: *Detailed Synchronization Waveform Regions.* The period begins with the camera being externally start triggered to light-sheet scanning such that it coincides with the linear scan region of the galvanometers. After completing the scan, the camera reads out to the data acquisition computer via a camera link frame grabber and the galvanometers are reset. This reset process incorporates the flyback process and acceleration back produce a linear scan region for the subsequent period.

4.2.2 Hardware Control

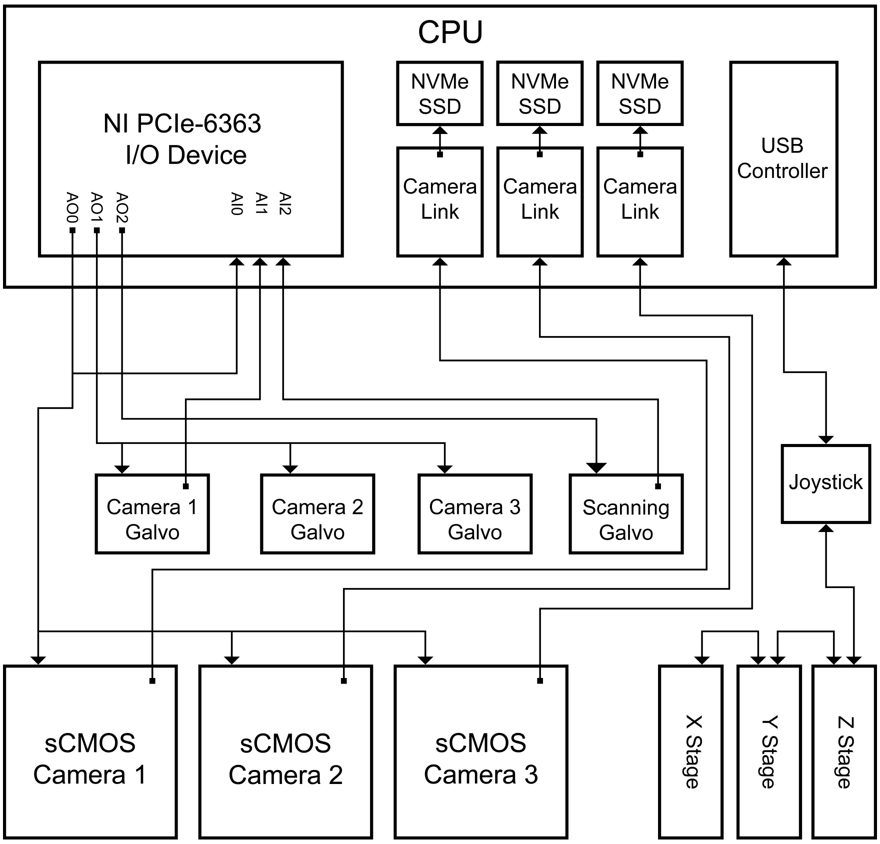
CPU
NI PCIe-6363
I/O Device
AO0
AO1
AO2
AI0
AI1
AI2
NVMe SSD
NVMe SSD
NVMe SSD
Camera Link
Camera Link
Camera Link
USB Controller
Joystick
Camera 1 Galvo
Camera 2 Galvo
Camera 3 Galvo
Scanning Galvo
sCMOS Camera 1
sCMOS Camera 2
sCMOS Camera 3
X Stage
Y Stage
Z Stage

Figure 4.7: *Wiring Schematic of Microscope.* Platform sTR4 Socket Threadripper 1950X CPU (Advanced Micro Devices, Santa Clara, CA, USA) workstation. Analog signals are created an NI PCIe-6363 multifunction I/O device. For camera control, a parallel TTL signal sent to three Hamamatsu Flash 4.0 V2s via AO0. The external start trigger activates the rolling shutter (light-sheet mode) of the sCMOS sensor which is synchronized with the "camera" and "scanning" galvanometers linear scan regions. The resulting image is captured via three FireBird Camera Link Frame Grabbers (1xCLD-2PE8) and sent to independent Samsung 970 PRO NVMe SSDs. AO2 controls the field scanning galvanometer with variable amplitude. AO1 sends scan signal to three camera galvanometers. 3-dimensional motorized stage is connected in series for each dimension along with a joystick connected to the computer via USB for software control. One of the camera galvo's, the scanning galvo, and the TTL signal sent to the cameras are monitored via the analog inputs (AI0-AI2).

CHAPTER 5

Results

5.1 Spatial Resolution

One pre-requisite to understand the optical performance of a system is to empirically calculate the point spread function of the system. In Section 2.2, the resolution of an optical system were given. Namely, the lateral and axial resolutions of the system are governed by the following two equations, respectively,

$$d_{lateral} = \frac{\lambda}{2NA}, \tag{5.1}$$

$$d_{axial} = \frac{2\lambda}{NA^2}. \tag{5.2}$$

5.1.1 Lateral and Axial Resolution

To conduct an analysis of the optical performance, 100 nm fluorescent beads, with a 488 nm excitation wavelength and emission wavelength peak of 507 nm, were imaged using a Nikon 40X 0.8 NA objective (Nikon Inc., Shinagawa, Tokyo, Japan). The number of beads image was 10 per image plane and the point spread function was calculated using a Gaussian profile fit to the intensity produced in all three dimensions. Following the previously mentioned equations should have a theoretical resolution of,

$$d_{lateral,theo} = \frac{\lambda}{2NA} = \frac{0.5\mu m}{2 * 0.8} = 0.3\mu m, \tag{5.3}$$

$$d_{axial,theo} = \frac{2\lambda}{NA^2} = \frac{2 * 0.5\mu m}{0.8^2} = 1.6\mu m, \tag{5.4}$$

Where theoretical lateral resolution is in both the X- and Y-dimensions and the theoretical axial resolution is in the Z-dimension. After entering the remapping cycle and the first plane imaged, the point spread function of the fluorescent beads was found to be,

$$d_{x,exp} = 0.7\mu m, \tag{5.5}$$

$$d_{y,exp} = 1.1\mu m, \tag{5.6}$$

$$d_{z,exp} = 1.6\mu m. \tag{5.7}$$

Overall, it is expected that point spread function should spread as a function of image relaying by imperfect lenses. In addition, it is found that the X-dimension is much closer to the theoretical minimum and only deviates by a factor of 2, compared to the Y-dimension which has an elongation factor of approximately 3. As for the axial dimension, it is found that the point spread function retains the theoretical minimum, which is quite surprising and most like also due to the confocality (optical sectioning) of the system. See Figure 5.1. It should be noted that in order to retain maximum transmission, the confocality of the system was limited to only block out light after the first dark fringe.

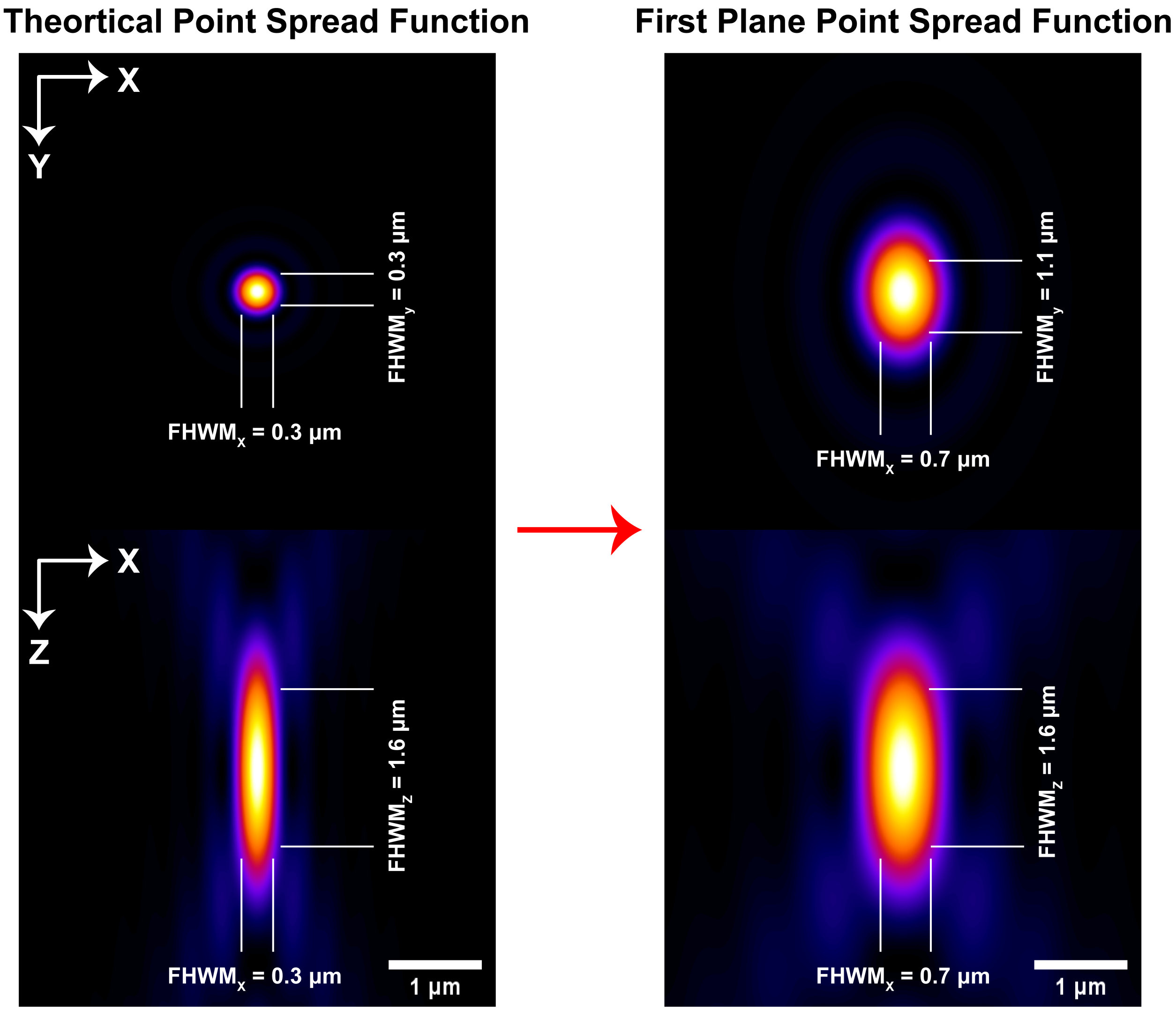
Theortical Point Spread Function
First Plane Point Spread Function
X
Y
FHWM$_y$ = 0.3 µm
FHWM$_x$ = 0.3 µm
X
Z
FHWM$_z$ = 1.6 µm
FHWM$_x$ = 0.3 µm
1 µm
FHWM$_y$ = 1.1 µm
FHWM$_x$ = 0.7 µm
FHWM$_z$ = 1.6 µm
FHWM$_x$ = 0.7 µm
1 µm

Figure 5.1: *Point Spread Function Theoretical vs Experimental.* After reaching the plane adjustment cycle, a comparison between the first image plane and the theoretical point spread functions is made. On the *left* the theoretical PSF generated using the Born and Wolf optical model using the ImageJ Plugin: PSF Generator by the EPFL Biomedical Imaging Group[6]. On the *right* is the average PSF of 100 nm fluorescent beads imaged image under 488 nm excitation. To obtain an average, beads were image using a Nikon 40X 0.8 NA objective. A Gaussian profile was fit to the intensity.

5.1.2 Resolution Depth Dependence

As the cyclic rearrangement continues for each subsequent image plane, the point spread function was calculate. Overall, the system retained near first plane resolutions, especially in the X-dimension where confocality was maintained. In the axial dimension, the PSF elongation was maintained to a minimum, again this is due to the optical sectioning of confocality. In the Y-dimension, it was observed that the PSF continued to elongate at a more rapid rate. See Figures 5.2 and 5.3.

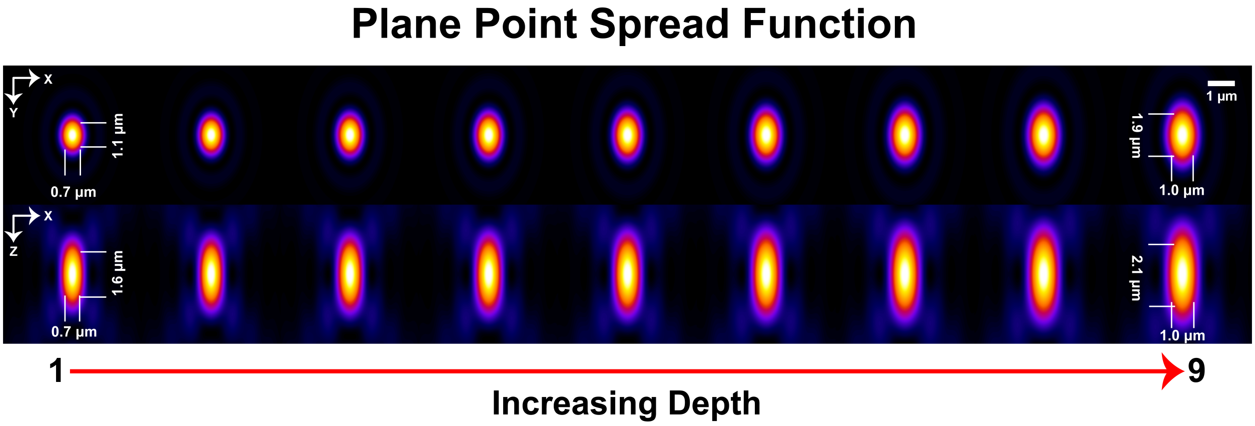

Figure 5.2: *Point Spread Function Depth Dependence.* 9 total image planes were imaged onto 3 separate sCMOS cameras. Due to the cyclic rearrangement and image relay process, the point spread function is bound to increase as a function of number of relays. For the 9 images planes, image resolution in all 3 dimensions had a linear relation to imaged depth. Reconstructed averages of the PSF in XY and XZ projections are displayed as a function of "increasing depth" or conversely, the number of increasing relays the image has undergone from left to right.

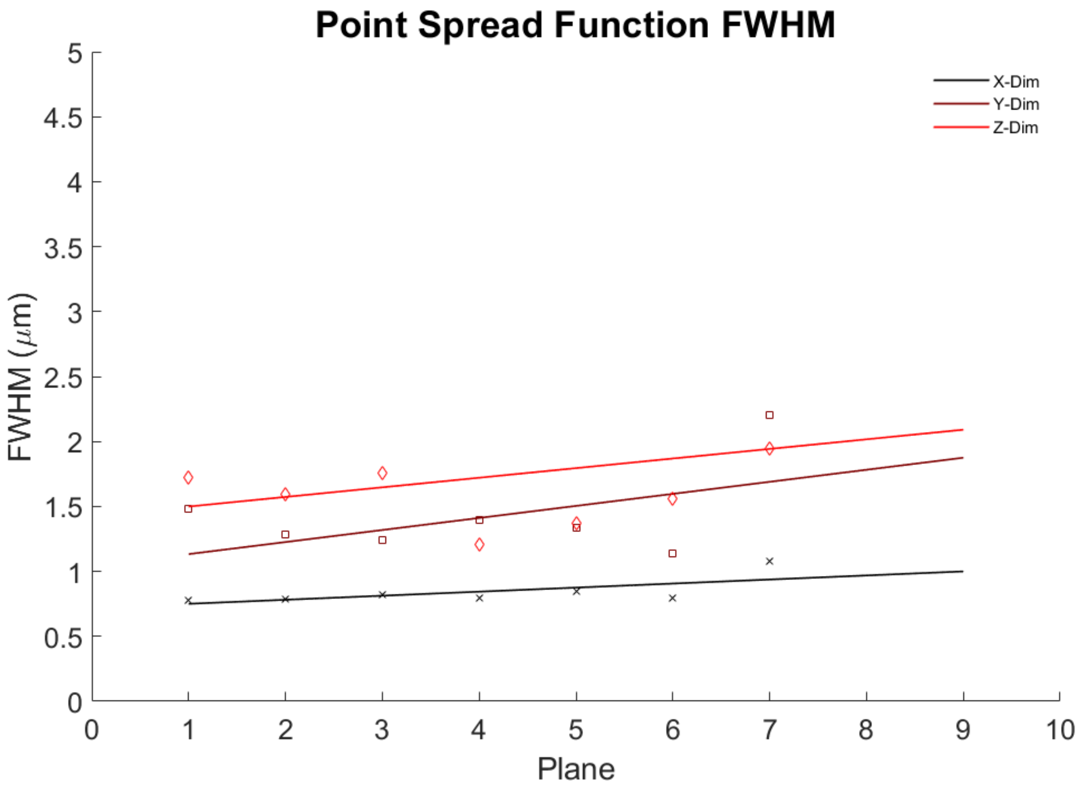

Figure 5.3: *Plane Dependence Spatial Resolution.* 100 nm fluorescent microspheres were imaged to determine the change in spatial resolution as a function of imaged plane. The imaging objective was a Nikon CFI Apo NIR 40X W, with an NA of 0.8. There is a linear dependence on the spatial resolution of the system and planes for all dimensions. Due to the confocality of the system, the least varying resolution is found in the x-dimension, with overall submicron resolution obtained. The y-dimensions shows a slightly larger over resolution and the function has an overall larger increase as a function plane. The axial dimension, z, also an increasing dependence on plane with the best axial resolution occurring at the initial plane.

5.2 Photon Efficiency

On account of the power loss from the illumination beam multiplexing and they image relay around the cycle, the intensity at the image sensor for each image plane decays. Below in Figure 5.4, the theoretical intensity at the image sensor is plotted as a function of both the multiplexing intensity loss and the image relay loss. Given the > 0.98 transmission coefficient of the lenses and > 0.99 reflection coefficient of the mirrors, the largest intensity determinant is the beam multiplexing itself. In addition, the measured intensities at the sensor compared to the intensity at the sample for each image plane experimentally shows that the major contributor of intensity discrepancy between the planes is the illumination multiplexing itself. The relay units only contribute a marginal decrease in the intensity at the image sensor. This indicates that if the illumination intensity profiles are adjusted such that they are more even, then the images captured could become more uniform. This can be achieved using a more clever multiplexing scheme, or by using a linear variable neutral density filter at a conjugate image plane after multiplexing is performed.

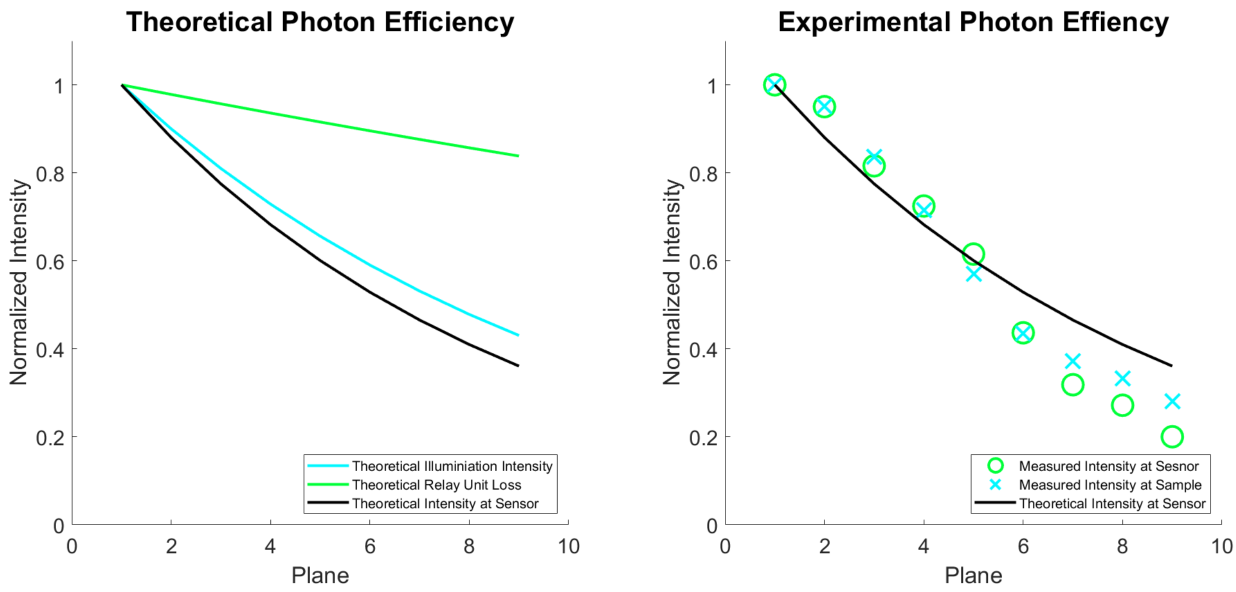

Figure 5.4: *TranSIM Photon Efficiency.* On the left, the calculated normalized intensity produced by illumination beam multiplexing, relay unit loss, and the overall theoretical normalized intensity at the image sensors. On the right, the measured normalized intensity at the sample, and at the image sensors, compared to the theoretical normalized intensity at the sensors. Note that the measured intensities at the sensor deviate from the theoretical, but this can be attributed to the fact that the illumination intensities did not follow the theoretical and began to decay faster after the fifth image plane.

5.3 Melanoma Cells Imaging

The main purpose of *TranSIM* is to image biological data. The axial separation for this imaging was set to 20 μm per plane. The imaging objective was a Nikon 16X CFI LWD Plan Fluorite Objective (Nikon Inc., Shinagawa, Tokyo, Japan), 0.80 NA objective with an effective magnification of 8X, resulting in a field of view per image plane of 554 μm $\times$ 374 μm. Additionally, it can be seen qualitatively that the overall intensity of each frame decreases as a function of depth, where the top plane is indicated -80μm on the top left corner. See Figure 5.5.

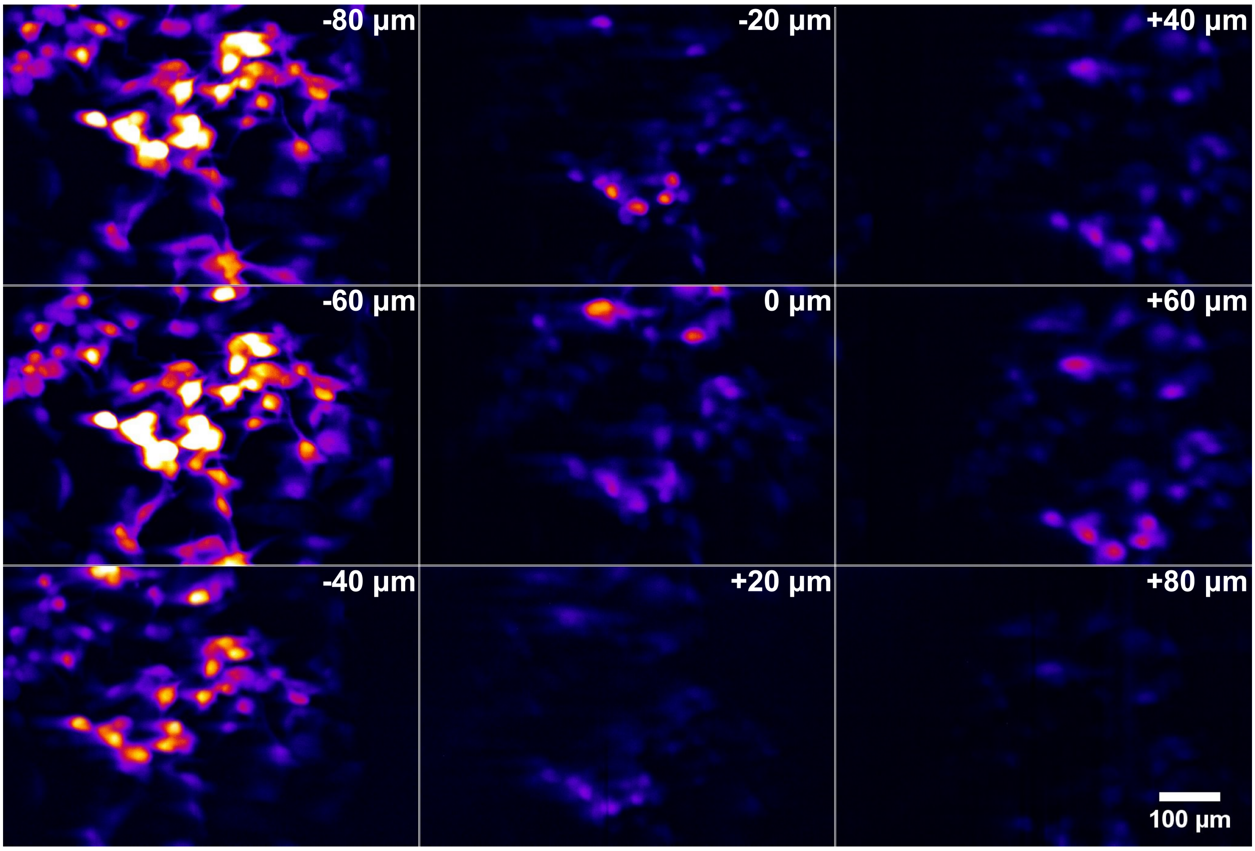

Figure 5.5: *GFP Tagged Melanoma Cells.* Each plane has an axial spatial separation of 20 μm and imaged using a Nikon 16X CFI LWD Plan Fluorite Objective, 0.80 NA objective with an effective magnification of 8X. NAOMM-1-GFP human uveal melanoma cells, which endogenously express GFP in the cytoplasm, were received from Dr. Samar Alsafadi of Curie Institute (Paris). Cells were maintained in RPMI 1640 (Gibco 21875-034) containing 10% fetal bovine serum and 1% Pen-Strep (Gibco 15140-122), on poly-d-lysine coated dishes in a 37°C, 5% CO_2 incubator. Cells were fixed for 20 minutes with 4% paraformaldehyde at $40\tilde{7}0$% con-fluency, leaving space to spread the cells into uniquely identifiable XY positions. Following fixation, cells were rinsed with and kept in 1x PBS.

5.4 *Caenorhabditis elegans* Imaging

After establishing a static biological fluorescent signal, *Caenorhabditis elegans* (*C. elegans*), was imaged in motion. This particular strain of *C. elegans* expresses a the calcium dynamic variant of GFP, GCaMP3, an older variant of the GCaMP6s/f discussed in section 2.2.3, and cultured to express in the muscles. In this study, the system was adjusted such that the image planes were separated only by 10 μm per plane due to the smaller cross-sectional area of the nematode. A single time volumetric snap-shop is shown in Figure 5.6. In Figure 5.7, a 3D rendering of the nematode after rough adjustment of parallelipiped translation caused by the illumination and subsequent detection.

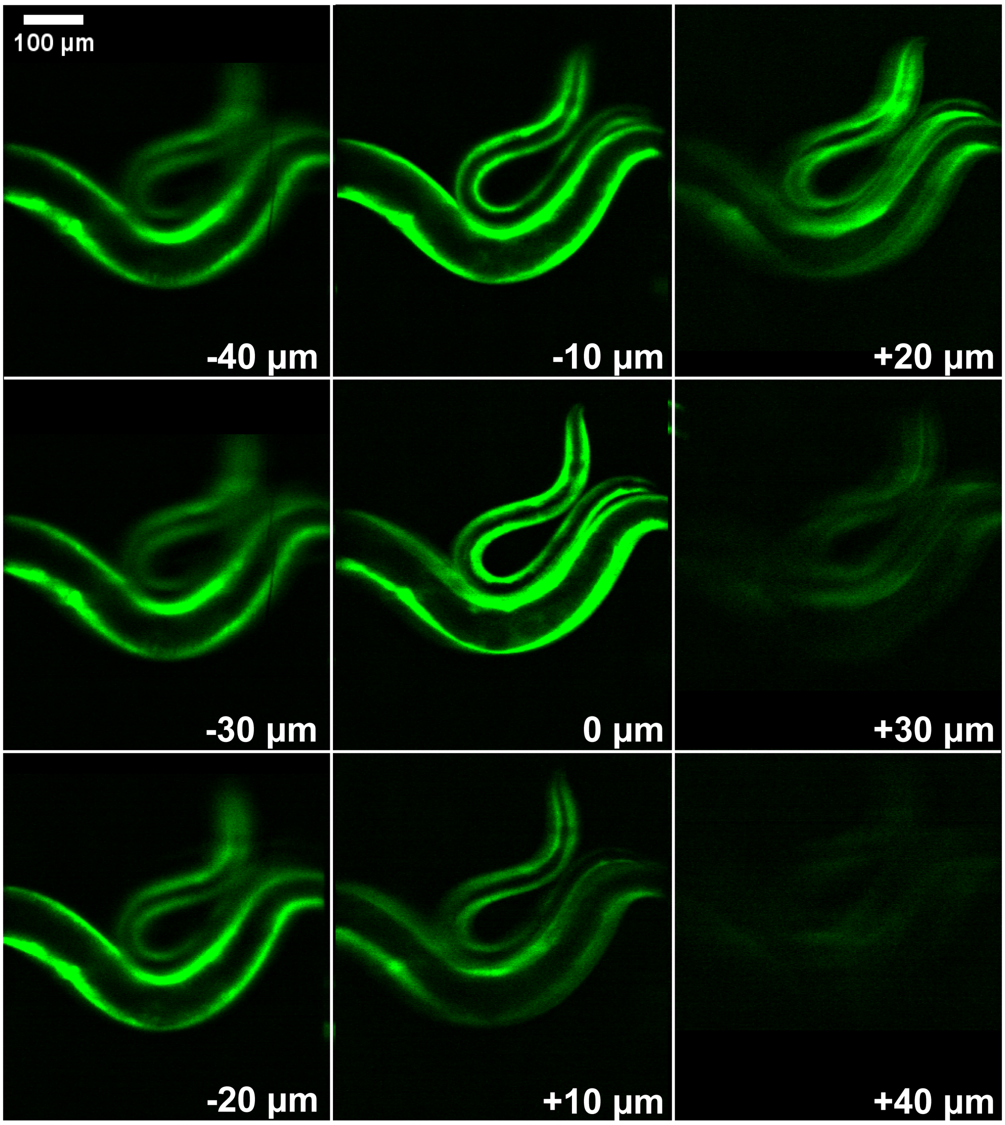
100 µm
-40 µm
-10 µm
+20 µm
-30 µm
0 µm
+30 µm
-20 µm
+10 µm
+40 µm

Figure 5.6: *GCaMP3 Encoded C. elegans.* Ca^{2+} indicator expresses in the muscles highlighted by bright fluorescence on the walls of the nematode. Single time frame. Captured at 200 HZ. Samples courtesy of Dr. Pavak Shah UCLA.

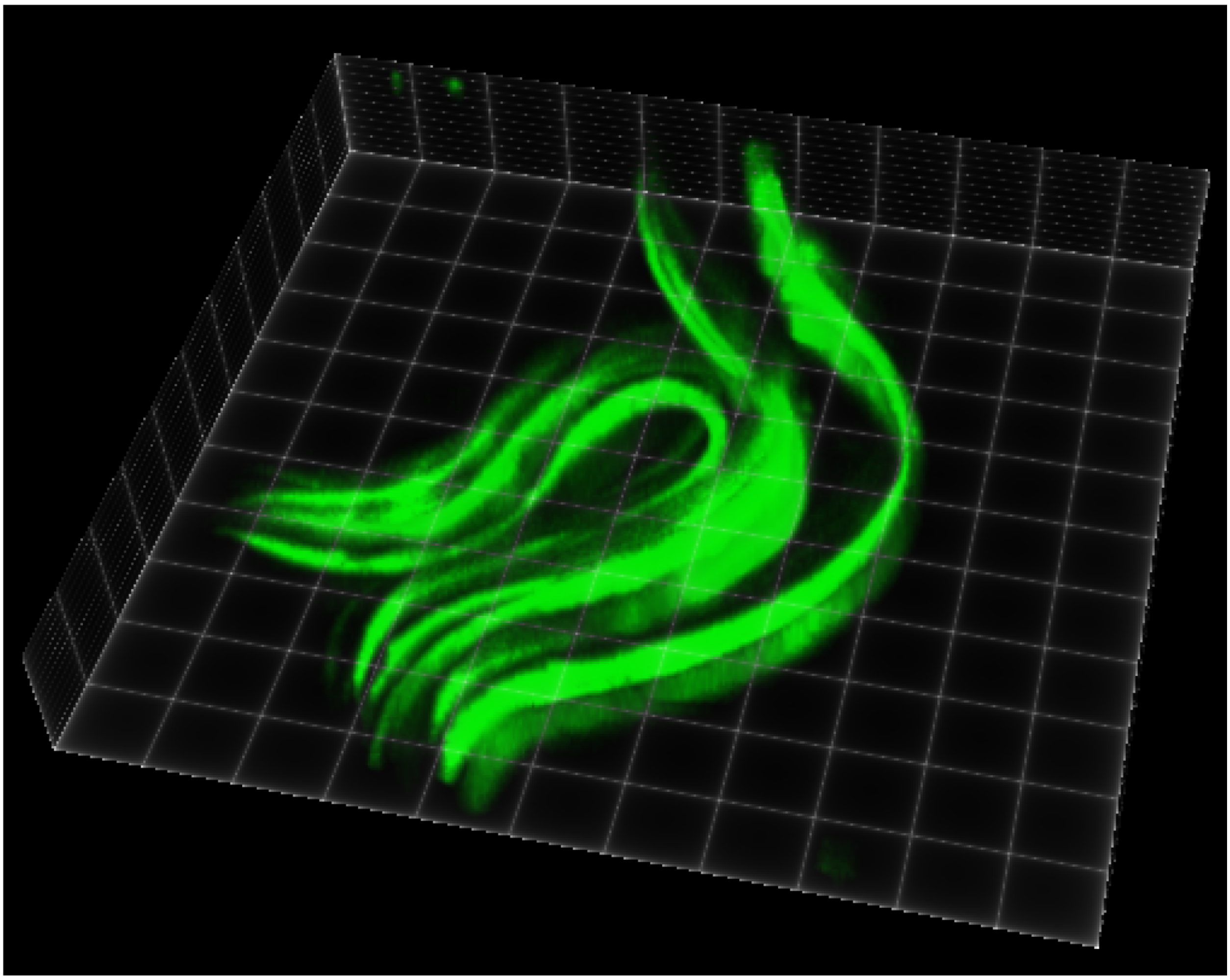

Figure 5.7: *3D Render of C. elegans.* Single volume rendition created in ClearVolume, Royer et al. (2015)[7]. Samples courtesy of Dr. Pavak Shah UCLA.

5.5 *Danio rerio* Imaging

Danio rerio, or more commonly known as *Zebrafish*, is a highly evolved vertebrate animal that exhibits high functioning processes with clear homologs to Humans. For example, the Optic Tectum (OT) is a direct homolog with a Human's Superior Colliculus (SC). To the OT, there is signal transfer that comes primarily from the retinas of the fish. In Humans, the circuit is much more complex before it reaches the SC. Recent studies indicate that spontaneous activity occurs in the Optic Tectum in a sensory deprived environment that has high correlation with non-deprive visual environments, Ramano et al. (2018)[37] and Marachlian et al. (2018)[38]. This points to the possibility that the fish is spontaneous creating visual experiences that have a basis in events that have not occurred and/or previous experiences. The study was not conclusive in this analysis. In addition, research shows spontaneous retinal waves propagate with a mean speed of 22.6 ± 0.5 μm/s, Zhang et al. (2016)[39]. This wave propagation speed was measured be by examining the wavefront location from start to fish and dividing by the time it took to propagate that distance.

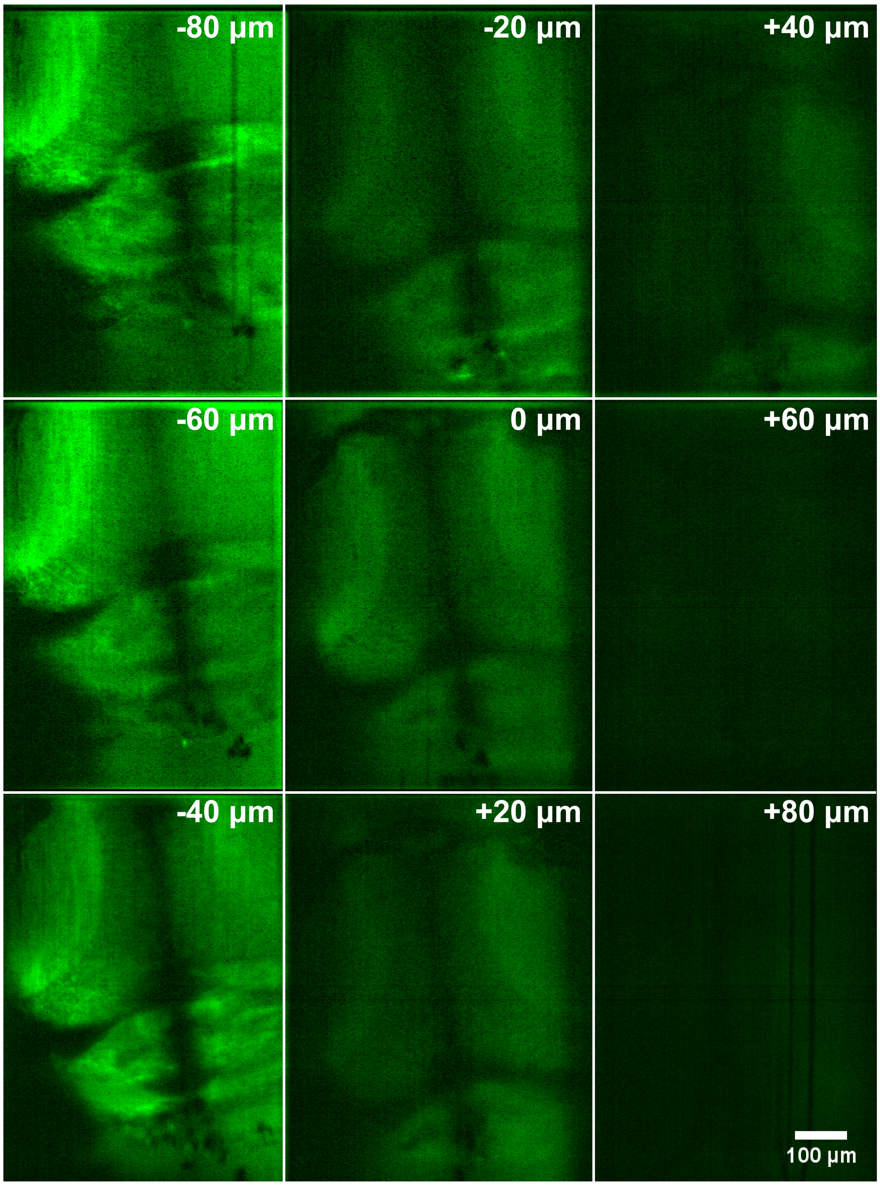

Figure 5.8: *GCaMP6s Encoded Danio Rerio 1.* Each plane has an axial spatial separation of 40 μm and imaged using a Nikon 16X CFI LWD Plan Fluorite Objective, 0.80 NA objective with an effective magnification of 8X. The voluemtric rate of imaging is 200 VPS with a field of view per image plane of 554 μm $\times$ 374 μm. The fish was held in place for imaging using a 2.5% by volume agarose mixture for near refractive index matching imaging. In addition, most of the agarose that lie on top of the brain region was removed as to reduce the agarose layer excitation and emission light had to travel through.

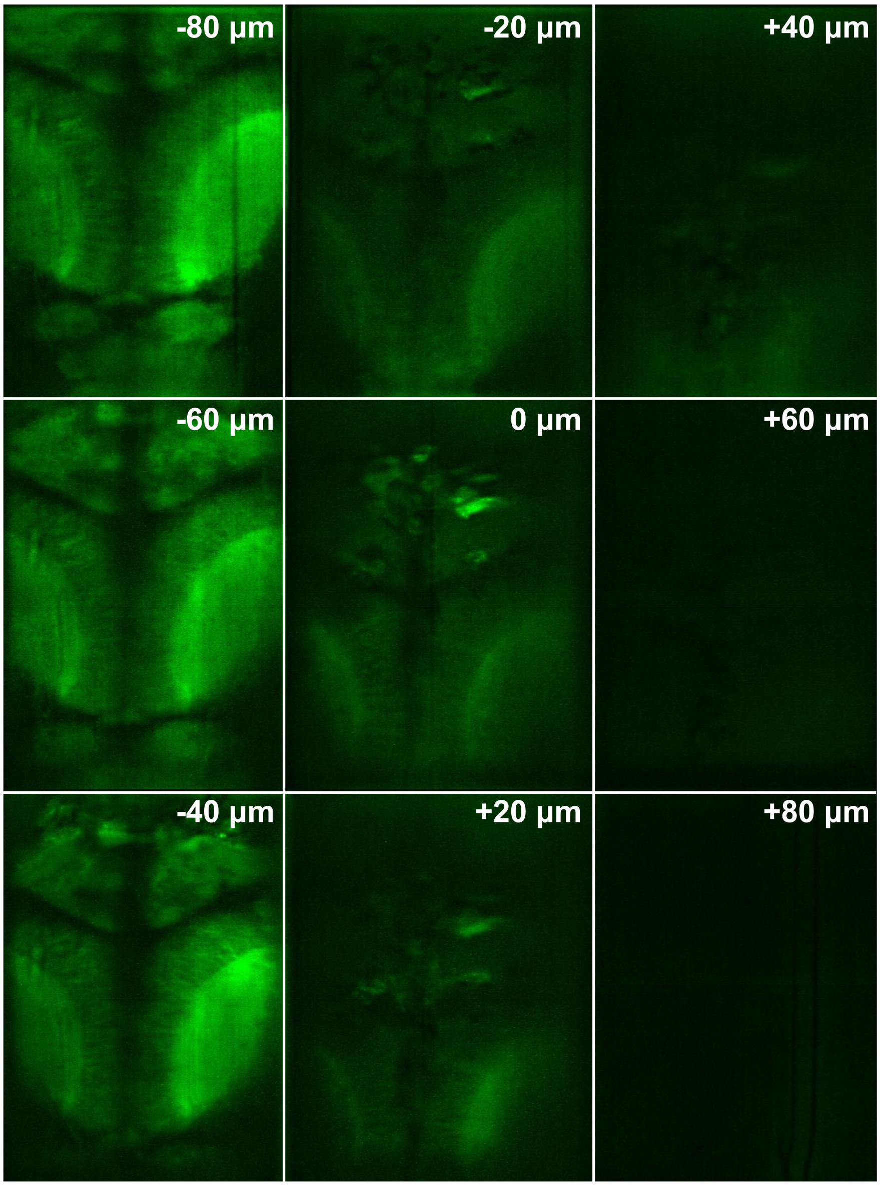

Figure 5.9: *GCaMP6s Encoded Danio Rerio. 2* Each plane has an axial spatial separation of 40 μm and imaged using a Nikon 16X CFI LWD Plan Fluorite Objective, 0.80 NA objective with an effective magnification of 8X. The voluemtric rate of imaging is 200 VPS with a field of view per image plane of 554 μm × 374 μm. The fish was held in place for imaging using a 2.5% by volume agarose mixture for near refractive index matching imaging. In addition, most of the agarose that lie on top of the brain region was removed as to reduce the agarose layer excitation and emission light had to travel through.

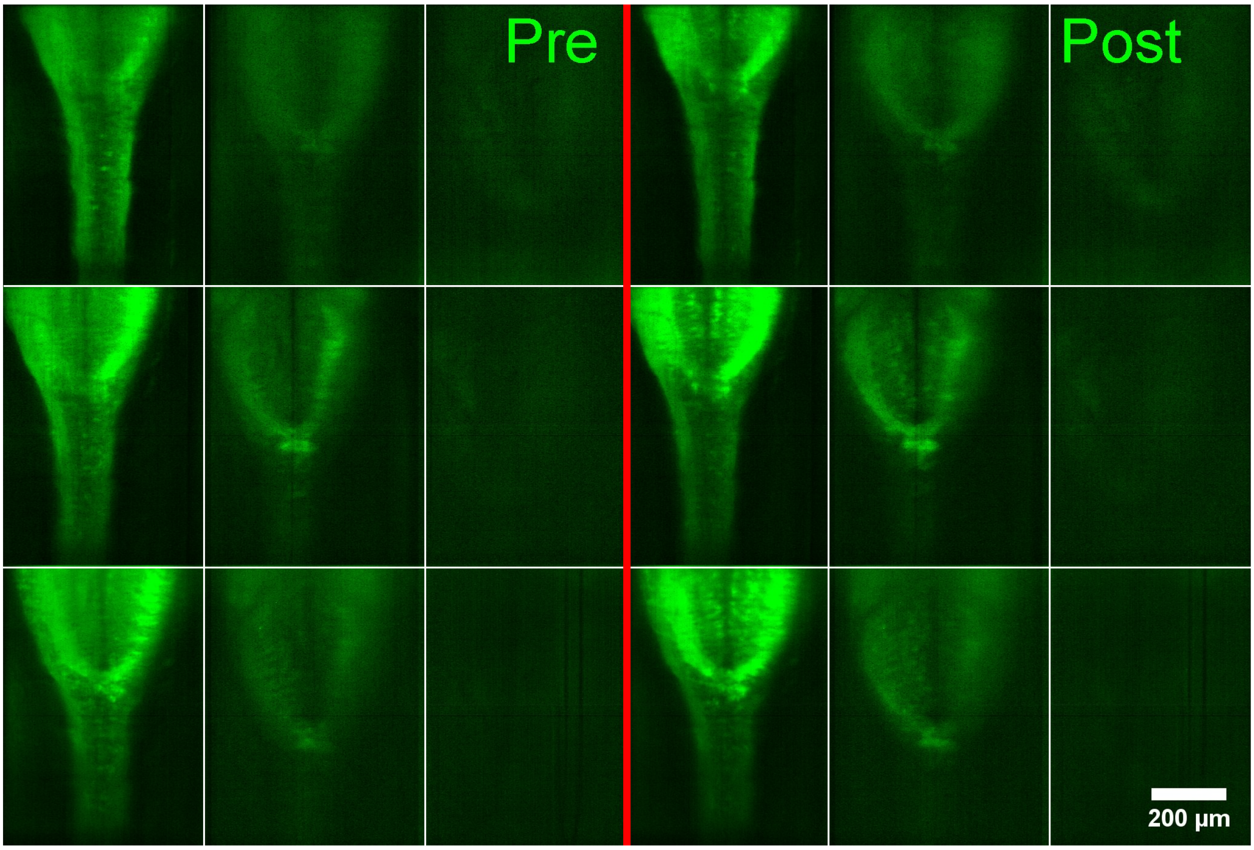

Figure 5.10: *Mustard Oil Induced Neural Activation of Danio rerio.* In order to induce substantial brain activity, mustard oil, an irritant, was injected into the water reservoir where the fish was held in place using an agarose bed. On the *left*, is a snap shot of the pre-mustard oil neural activity. On the *right*, mustard oil induced neural activation can be seen by higher overall signal strength. Recreation of experiment done by Roberts et al (2020)[8]

5.5.1 Intra-planar Neural Signal Propagation.

In order to demonstrate the power of *TranSIM*, neural analysis was conducted by means of single plane neural signal propagation, Figure 5.11. It is seen that intra-planar propagation occurs. GCaMP6, Ca^{2+}, leading edge signal, starting at the Neurophil (NP), the signal propagates inward towards the Periventricular Layer (PVL). Single locations distanced 40 μm apart were analyzed and plotted. Also plotted were individual sections of the overall signal where it shows that the time difference activation between difference location are on the order of 100 ms from start to end (NP → PVL). The resulting wavefront propagation speed was measured to be 1200 μm/s, which is several orders of magnitude faster than those observed in the retina by Zhang et al., measured at 22.6 ± 0.5 μm/s[39], although they are fundamentally in different regions of the brain.

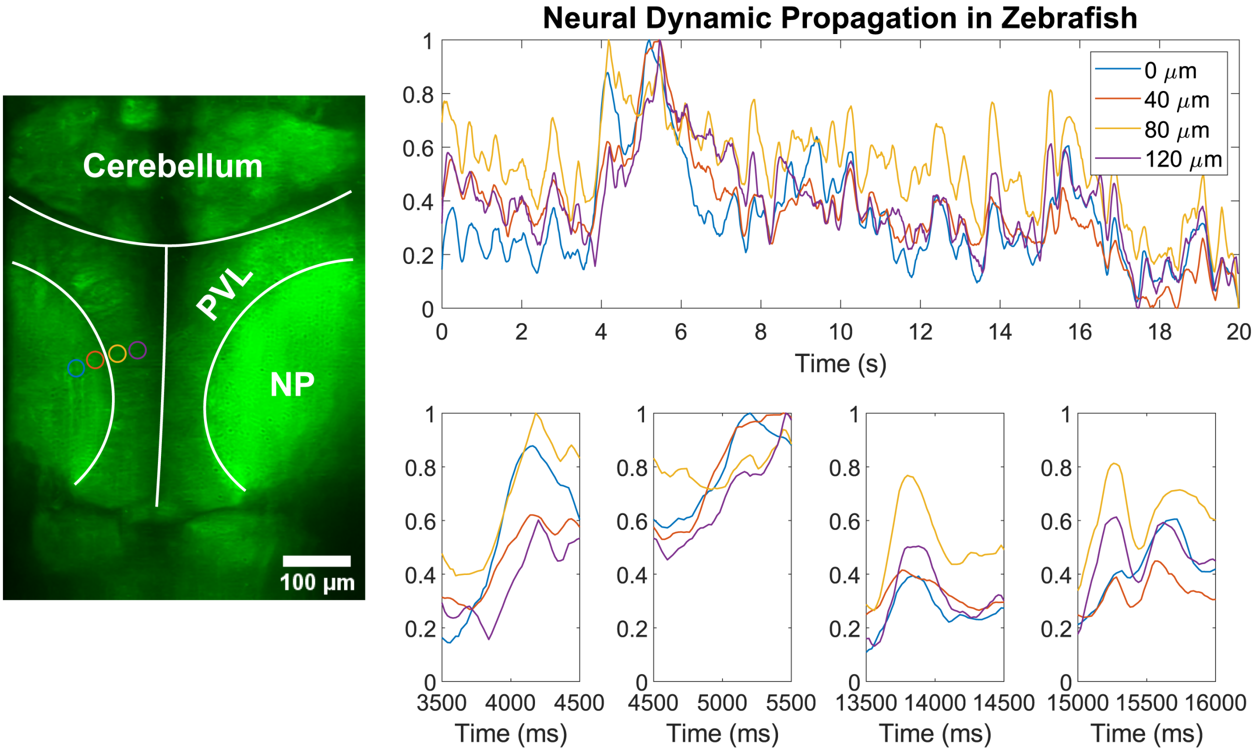

Figure 5.11: *Neural Signal Propagation in Danio rerio.* Imaged at 200 VPS, the single image plane was analyzed to show signal propagation. 4 locations were chosen from visual inspection of neural activation. Analysis shows that the signal propagates inwards from the Neurophil (NP) to the Periventricular Layer (PVL). The spatial separation of each location is 40 μm. Temporal sequence shows that from the first location inside the NP to the central PVL location, there is a $\sim$100 ms delay in the leading edge activation. The wavefront propagation speed was measured to be 1200 μm/s.

5.5.2 Inter-planar Neural Signal Propagation

Following analysis of intra-planar propagation which has been conducted in previous research, inter-planer propagation was also visualized. From the Mustard Oil neural activation experiment, 3 separate planes were selected, 40 μm apart. Similarly, to the intra-planar propagation, signal also shows depth time dependence governing same axial positioning. See Figure 5.12. Calcium wave propagation can be seen in Figure 5.13, where the wave begins at the top of the frame and continues backwards towards towards the tail of the fish, thereby inducing a tail bout in the fish.

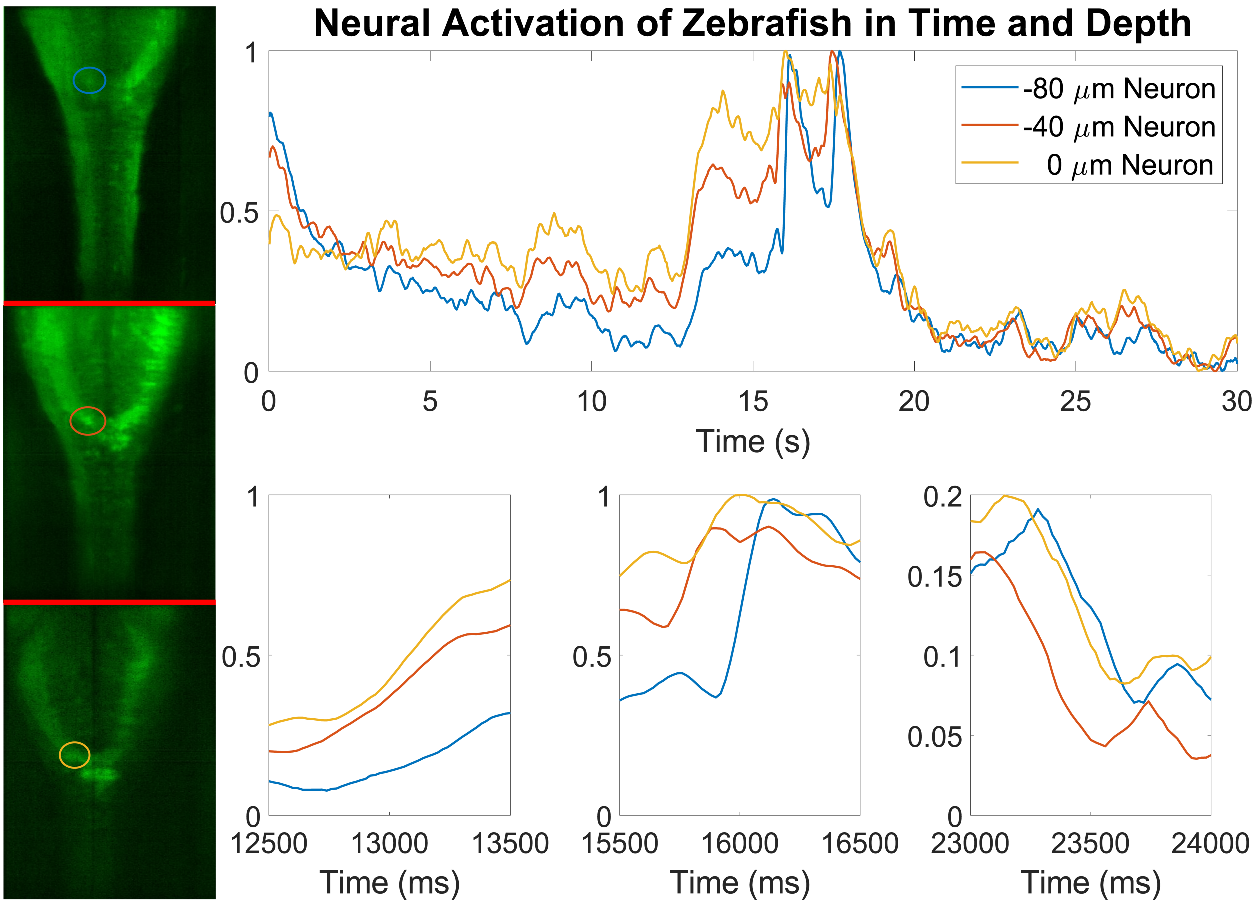

Figure 5.12: *Temporal Sequence at Various Depths.* The volumetric imaging rate is 200 VPS, resulting in a temporal resolution of 5 ms. Each plane shown is 40 μm apart. Overall signal from the three regions of interest are plotted in the top graph. Areas of interest indicated by their time frames are plotted below. Leading and falling edge signals indicate a temporal dependence from plane to plane.

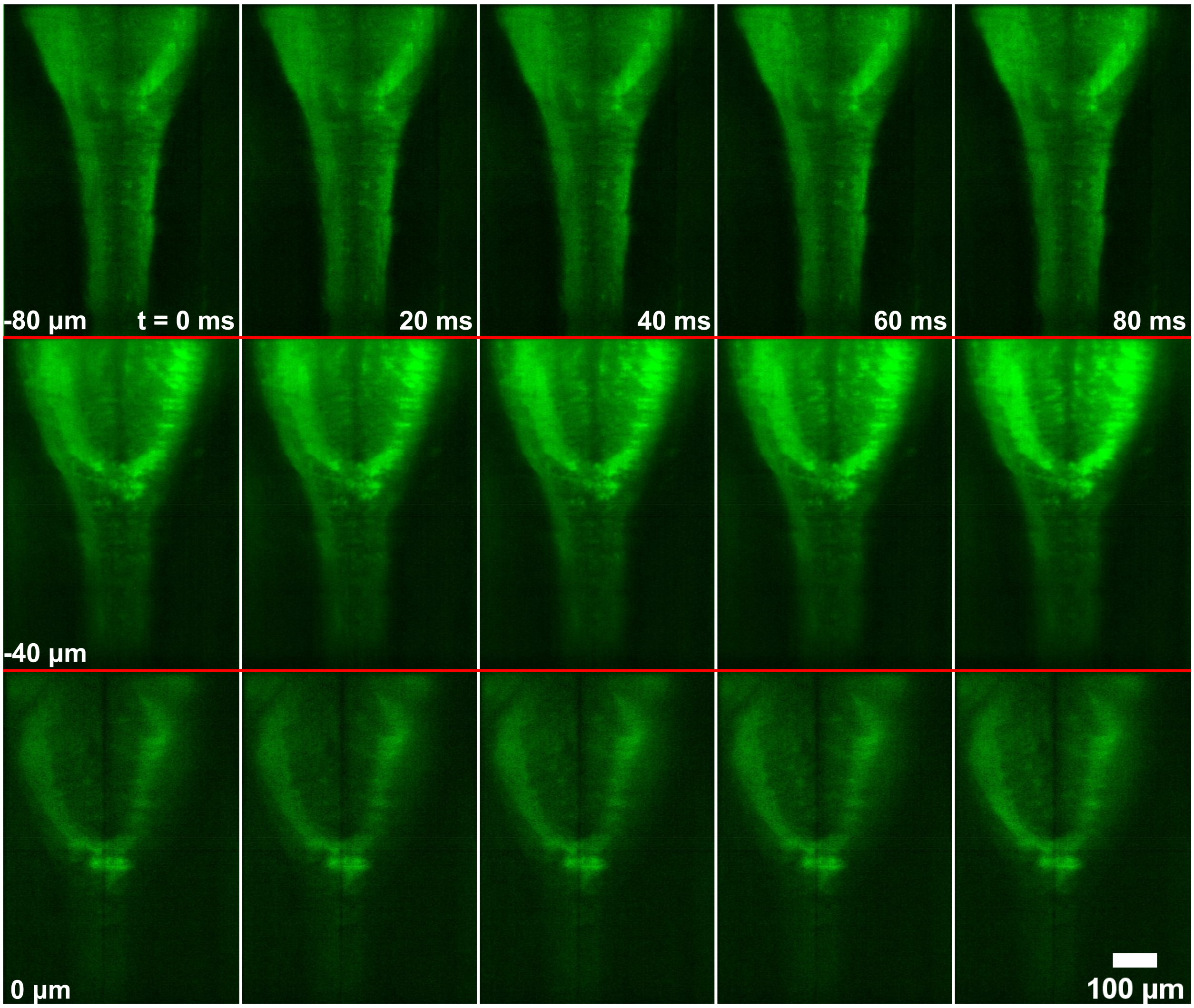
-80 µm
t = 0 ms
20 ms
40 ms
60 ms
80 ms
-40 µm
0 µm
100 µm

Figure 5.13: *Multi-plane Ca^{2+} Wave Propagation.* Three independent planes are shown spaced 40 μm apart, corresponding to the 1st, 3rd, and 5th image planes in the volume. Starting from the left column, at t = 0 ms, the wave begins at the top of each plane and propagates downward towards to tail of the fish, in the span of 80 ms, inducing a tail bout.

CHAPTER 6

Future Directions

The previous chapter demonstrates that *TranSIM* has the capability to image large volumes with fast temporal resolution with level micron resolution. However, in order to maximize the capability of the system, future work must be conducted. This chapter will focus on 4, and currently being explored, future work possibilities. With the implementation of these 4 future directions, *TranSIM* is bound aid research towards ground breaking discoveries. The open geometry, of the system allows for the incorporation of various bulky apparatuses, such as behavioral observation (6.1) and virtual reality (6.2). In addition, the optical and bandwidth performance of the system can be further improved with a by implementing a new illumination schema (6.3) and applying neural networks to regain the information lost in between the sparse planes (6.4). Lastly, with the advent of new genetically encoded voltage indicators (GEVIs) (6.5), like Voltron, and its positive variant, Positron, the era of imaging neural activation beyond the standard slow kinetics of GCaMP and near its true voltage oscillations is upon us.

6.1 Behavioral Observation

Correlating the behavioral motions of dynamics of Danio rerio to the neural activity is of utmost importance to the field of Neuroscience. In addition to *TranSIM*, an eye-tracking algorithm with millisecond written in LabVIEW has been create and awaiting implementation for a more complete system to study complex neurodynamics. In Figure 6.1, a screen shot of the software is shown. Lastly, the tail bouts of the fish can also be analyzed to determine the direction the fish would take given the angle and amplitude of the tail deflection.

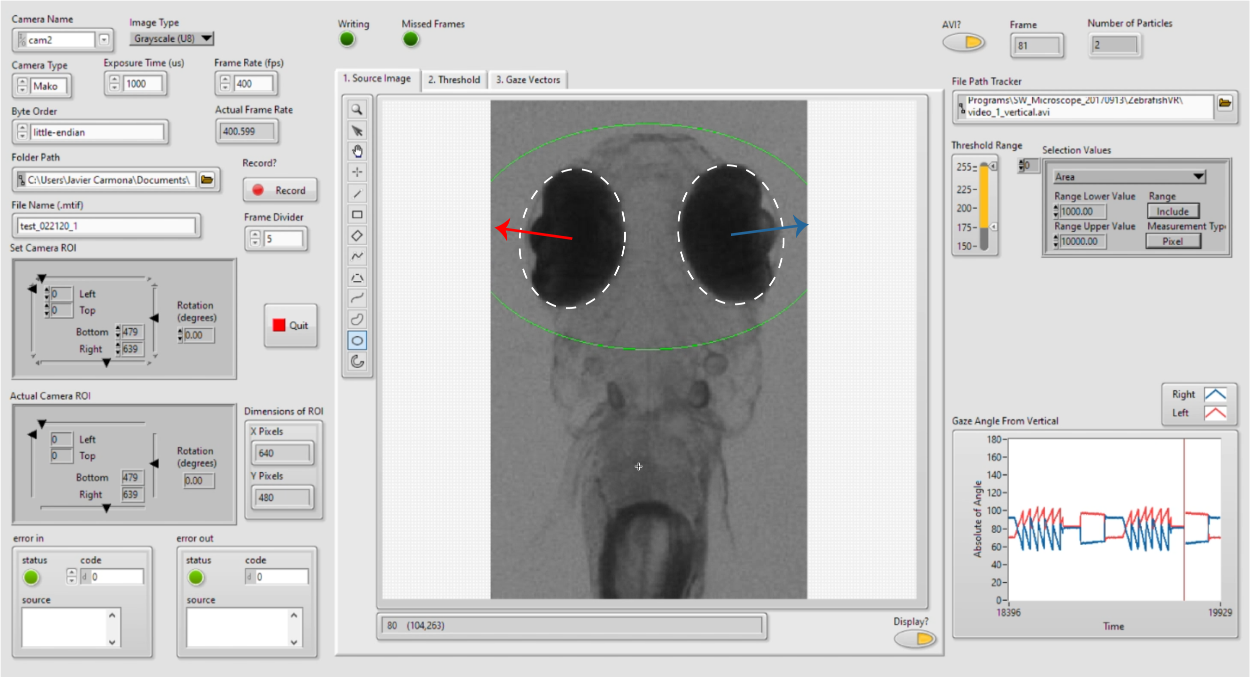
Camera Name: cam2
Image Type: Grayscale (U8)
Camera Type: Mako
Exposure Time (us): 1000
Frame Rate (fps): 400
Byte Order: little-endian
Actual Frame Rate: 400.599
Folder Path: C:\Users\Javier Carmona\Documents\
File Name (.mtif): test_022120_1
Frame Divider: 5
Set Camera ROI: Left 0, Top 0, Bottom 479, Right 639, Rotation (degrees) 0.00
Actual Camera ROI: Left 0, Top 0, Bottom 479, Right 639, Rotation (degrees) 0.00
Dimensions of ROI: X Pixels 640, Y Pixels 480
error in: status ●, code 0, source
error out: status ●, code 0, source
Frame: 81
Number of Particles: 2
File Path Tracker: Programs\SW_Microscope_20170913\ZebrafishVR\video_1_vertical.avi
Selection Values: 0, Area, Range Lower Value 1000.00, Range Include, Range Upper Value 10000.00, Measurement Type Pixel
80 (104,263)

Writing
Missed Frames
Record?
Record
Quit
1. Source Image
2. Threshold
3. Gaze Vectors
AVI?
Display?
Threshold Range
255
225
200
175
150
Gaze Angle From Vertical
Right
Left
Absolute of Angle
180
160
140
120
100
80
60
40
20
0
18396
19929
Time

Figure 6.1: *Zebrafish Eye Tracking Software.* Custom real-time eye tracking software made in LabVIEW. Maximum operational eye tracking speed determined by sensor. Angular resolution of $\leq 0.5^{o}$. Tested at frames rates of up to 550 FPS with Allied Vision Mako U-029B USB 3.0, monochrome camera, at full frame, 640 pixels × 480 pixels.

6.2 Virtual Reality

In development, is a virtual reality system, that aims to be as responsive and immersive to what a wild zebrafish would experience. In combination with eye-tracking and the real tail bout analysis, the virtual reality system can create a feed-back loop system where the scenery can be adjusted to reflect the behavioral process the fish is intending. Also, zebrafish exhibit 2 main behavioral driving modes, predator and prey modes. The virtual reality system can be programmed to display such events.

6.3 Improved Illumination

Although *TranSIM* has relatively decent spatial resolutions, the requirement to go further drives development. In Figure 6.2 *left*, is a proposed illumination method that should increase spatial resolution. By colliding two Gaussian beams from the maximum angle allowed by the aperture, the system transforms into a more photon efficient system that can help reduce common concerns in microscopy, photobleaching and phototoxicity. *TranSIM's* current illumination mechanism is a single gaussian sheet created by a cylindrical lens. Due to the board illumination of caused by this type of illumination, biological samples that are prone to phototoxicity and photobleaching might suffer needlessly. To get around this issue, illumination must approach the gentle illumination seen in orthogonal geometry light sheet systems where the photon efficiency of illumination is much higher. Additionally, in Figure 6.2 *right*, it is also proposed a method by which to increase the depth even illumination, as it was shown in section 5.1.2 that the depth information remained relatively close to theoretical minimum. In some instances, it is a good idea to capture more out of plane information in a maximum projection manner.

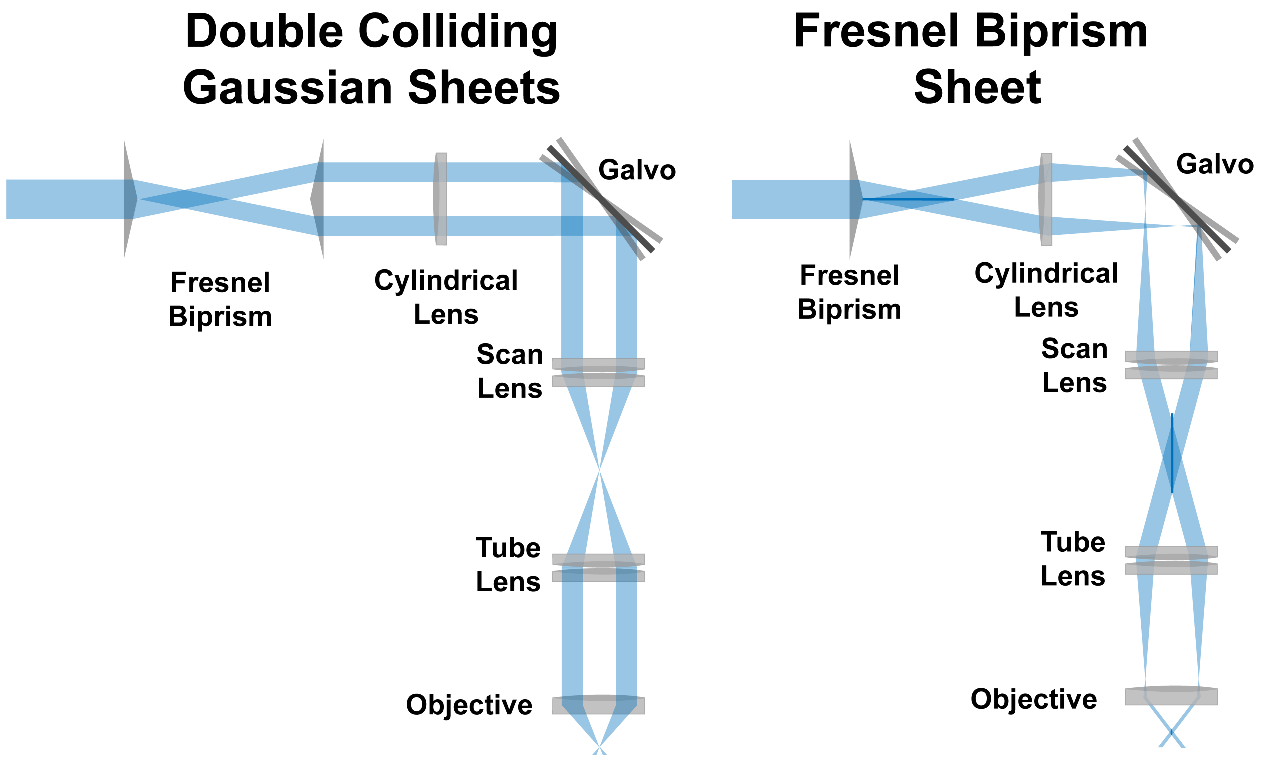
Double Colliding Gaussian Sheets
Fresnel Biprism
Cylindrical Lens
Galvo
Scan Lens
Tube Lens
Objective
Fresnel Biprism Sheet
Fresnel Biprism
Cylindrical Lens
Galvo
Scan Lens
Tube Lens
Objective

Figure 6.2: *Proposed Illumination. Transverse-Sheet Illumination Microscopy* has in its current design, a single Gaussian sheet illumination mechanism, multiplexed 9 times. These multiplexed beams have a broad colliding angle, which in turn causes phototoxicity and photobleaching at the sample. To reduce said effects, two additional illumination methods are proposed in order to clear as much of the area being illuminated from light contamination. On the *left*, is a double Gaussian sheet method by which to collide nearly orthogonal sheets to a single location thereby clearing the sample light contamination from the top and bottom of the collision location. On the *right*, is an increased depth illumination method and create a long uniform illumination sheet similar to those created in Bessel-Gauss Light Sheet Microscope by plane wave interference.

6.4 Deep-Z Application

In recent years, neural networks has become an invaluable tools to regain or reconstruct otherwise "lost" information. In section 3.6.1, Light Field Microscopy, shed light on a process by which to refocus out of focus light and obtain a 3D volume from 2D imaging methodologies. At its core, deconvolution is the driving for of the aforementioned system. Moving forward, neural networks, have advanced enough to by-pass this long and arduous process requiring apriori knowledge of the optical system. *Deep-Z*, Wu, et al.[40], circumvents all of this and instead relies on the training of a neural network to formulate a set of weights and biases to apply to future data-sets and reconstruct once "lost" or "convolved" information. In fact, the application of Deep-Z seems to be the natural evolution of *TranSIM*, which has by design large swaths of missing information. Deep-Z has shown the ability to refocus information from confocal systems in up to ± 10 μm. By carefully separating the planes of *TranSIM* to fall in the exact range, the information gaps that were once missing could closed. This would render true 3D volumes instead of the pseudo-volumes currently being image. See Figure 6.3.

With a Deep-Z implementation of TranSIM, the bandwidth of the combined system grows exponentially. Each plane can be multiplexed by 40 times, as was demonstrated by Wu, et al.[40], for 9 total planes, bringing the total pixel rate from 0.56 GPixels/second to a potentially 23.2 GPixels/second. Additionally, by improving the current imaging sensors to the latest commercially available, the pixel rates jump to a staggering 177.6 GPixels/second. Refer to Table 3.1. At these rates, entire brains for model organism can be captured temporally with electrophysiology type speeds, but with cellular resolution.

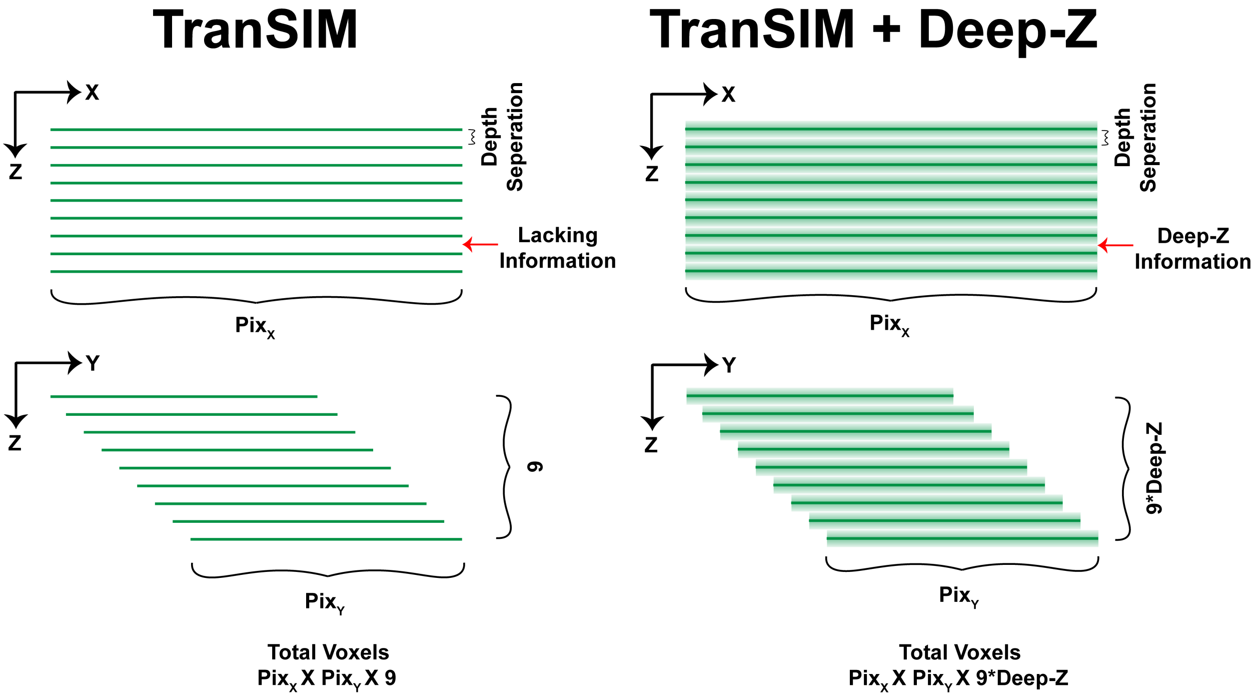
TranSIM
TranSIM + Deep-Z
X
Z
Depth Seperation
Lacking Information
Deep-Z Information
Pix$_X$
Y
9
9*Deep-Z
Pix$_Y$
Total Voxels
Pix$_X$ X Pix$_Y$ X 9
Pix$_X$ X Pix$_Y$ X 9*Deep-Z

Figure 6.3: *TranSIM with Deep-Z Propagation.* Due to the limited number of layers *TranSIM* can reliably capture, there is a trade-off between layer separation and total one wishes to image. However, both cannot be improved simultaneously. Instead, Deep-Z, a new depth refocusing microscopy method sheds light on the possibility of instead optimizing the axial separation and turning to neural networks to regain the out of focus/plane information and recreate a true 3D volume.

6.5 Genetically Encoded Voltage Indicators

Recently, Abdelfattah et al. (2019) [41] have created genetically encoded voltage indicators, or GEVIs, that allow animals a dye to bind to proteins permanently, which they have named Voltron. These dyes in turn have much faster kinetics than the traditional rhodopsins like GCaMP. However, major drawbacks include the the fact that they are not as bright as their only protein counterparts and the duration for which they can be image before bleaching. Furthermore, Abdelfattah et al. (2020) [42] have created a new version that has better overall peak brightness while also flipping the voltage indication and they have named this new GEVI Positron. With these GEVIs, we can now begin to monitor *Danio rerio* at near millisecond resolution over the entirety of its brain.

CHAPTER 7

Discussion and Conclusion

Using *Tranverse-Sheet Illumination Microscopy*, animals like *Danio rerio* at a 4-5 day old larvae stage, are imaged at 200 Hz in almost their entire volumetric brain profile of 750 μm × 400 μm × 250 μm. Given that each neuron occupies a spherical region with a 5-10 μm radius, there are approximately 10^5-10^6, all of which are activating in ensembles to process the their world with millisecond timing. Yet, one would expect that at such fast speeds, the trade-off would be spatial resolution. However, TranSIM takes advantage of previous imaging resolution retention methods and maintained near diffraction limit resolution that allows for single neurons to be imaged with a comfortable pixel area of about 20-100 pixels^2, garnering thousands of discernible neurons per image plane. The result is sparse but large volumes being imaged in 9 evenly separated slices, and thousands to tens of thousands of neurons being imaged simultaneously with near millisecond resolution.

In addition, the bandwidth limit currently imposed on TranSIM can be overcome with the utilization of newest generation sCMOS sensors that can increase to the total bandwidth of the system 2-10 Fold from an already respectable 0.56 GPixels/second to an unparalleled 4.33 GPixels/second. This implementation would by-pass any state-of-the-art system by nearly 4 times. See Table 3.1. Moreover, with the aid of novel neural network research, like Deep-Z, the already unparalleled speed could reach unforeseen speeds of 23.15 GPixels, with its current imaging sensors, and up to 177.55 GPixels/second with newest generation sensors; a 150-fold increase in the throughput compared to any system.

The way that TranSIM images, allows for such versatile future prospects. It paralleled processed the once parallel process of Line Scanning Confocal and Light Sheet microscopy into the third dimension, depth. In addition, it retained workable spatial resolution of 0.7

μm, 1.1 μm, 1.6 μm in x, y, and z, respectively. This spatial resolution retention allows for the imaging of thousands of neurons in zebrafish. Although, the major drawback of spatial gap between layers, which were from 10 μm to 20 μm, a solution has been brought forth that could remedy said problem with already proven techniques. In the end, I hope that this tool is put to use for the reason it was invented, and that is to study to highly complex neural dynamic processes of biological organisms.

REFERENCES

[1] Katsushi Arisaka and Laurent Bentolila. Trans-Sheet Illumination Microscopy (TranSIM) for decoding whole brain activity at submillisecond temporal resolution.

[2] Misha B. Ahrens, Michael B. Orger, Drew N. Robson, Jennifer M. Li, and Philipp J. Keller. Whole-brain functional imaging at cellular resolution using light-sheet microscopy. *Nature Methods*, 10(5):413–420, May 2013. Number: 5 Publisher: Nature Publishing Group.

[3] Venkatakaushik Voleti, Kripa B. Patel, Wenze Li, Citlali Perez Campos, Srinidhi Bharadwaj, Hang Yu, Caitlin Ford, Malte J. Casper, Richard Wenwei Yan, Wenxuan Liang, Chentao Wen, Koutarou D. Kimura, Kimara L. Targoff, and Elizabeth M. C. Hillman. Real-time volumetric microscopy of in vivo dynamics and large-scale samples with SCAPE 2.0. *Nature Methods*, 16(10):1054–1062, October 2019. Number: 10 Publisher: Nature Publishing Group.

[4] Bi-Chang Chen, Wesley R. Legant, Kai Wang, Lin Shao, Daniel E. Milkie, Michael W. Davidson, Chris Janetopoulos, Xufeng S. Wu, John A. Hammer, Zhe Liu, Brian P. English, Yuko Mimori-Kiyosue, Daniel P. Romero, Alex T. Ritter, Jennifer Lippincott-Schwartz, Lillian Fritz-Laylin, R. Dyche Mullins, Diana M. Mitchell, Joshua N. Bembenek, Anne-Cecile Reymann, Ralph Böhme, Stephan W. Grill, Jennifer T. Wang, Geraldine Seydoux, U. Serdar Tulu, Daniel P. Kiehart, and Eric Betzig. Lattice light-sheet microscopy: Imaging molecules to embryos at high spatiotemporal resolution. *Science*, 346(6208), October 2014. Publisher: American Association for the Advancement of Science Section: Research Article.

[5] Blake Madruga. *Design and Construction of a Rapidly-Reconfigurable SLM-Based Light Sheet Microscope*. PhD thesis, UCLA, 2018.

[6] BIG • PSF Generator.

[7] Loic A Royer, Martin Weigert, Ulrik Günther, Nicola Maghelli, Florian Jug, Ivo F Sbalzarini, and Eugene W Myers. ClearVolume: open-source live 3D visualization for light-sheet microscopy. *Nature Methods*, 12(6):480–481, June 2015.

[8] Adam C. Roberts, Joseph B. Alzagatiti, Duy T. Ly, Julia M. Chornak, Yuqi Ma, Asif Razee, Gohar Zavradyan, Umair Khan, Julia Lewis, Aishwarya Natarajan, Alisher Baibussinov, Jasmine Emtage, Meghna Komaranchath, Jared Richards, Michelle Hoang, Jason Alipio, Emma Laurent, Amit Kumar, C. S. Campbell, Rebecca Stark, Javier Carmona, Anjum Hussain, Courtney Scaramella, Jenan Husain, Reed Buck, Ava Jafarpour, Miguel Garcia, Steve Mendoza, Gerardo Sandoval, Brandon Agundez, Amanda Fink, Emily Deutsch, Sarah C. Hernandez, Katsushi Arisaka, and David L. Glanzman. Induction of Short-Term Sensitization by an Aversive Chemical Stimulus in Zebrafish Larvae. *eNeuro*, 7(6), November 2020. Publisher: Society for Neuroscience Section: Research Article: New Research.

[9] Owen Randlett, Caroline L. Wee, Eva A. Naumann, Onyeka Nnaemeka, David Schoppik, James E. Fitzgerald, Ruben Portugues, Alix M. B. Lacoste, Clemens Riegler, Florian Engert, and Alexander F. Schier. Whole-brain activity mapping onto a zebrafish brain atlas. *Nature Methods*, 12(11):1039–1046, November 2015. Number: 11 Publisher: Nature Publishing Group.

[10] Rainer Friedrich, Christel Genoud, and Adrian A. Wanner. Analyzing the structure and function of neuronal circuits in zebrafish. *Frontiers in Neural Circuits*, 7, 2013. Publisher: Frontiers.

[11] Olga I. Kahn, Philipp Schätzle, Dieudonnée van de Willige, Roderick P. Tas, Feline W. Lindhout, Sybren Portegies, Lukas C. Kapitein, and Casper C. Hoogenraad. APC2 controls dendrite development by promoting microtubule dynamics. *Nature Communications*, 9(1):2773, July 2018. Number: 1 Publisher: Nature Publishing Group.

[12] Adam D. Douglass, Sebastian Kraves, Karl Deisseroth, Alexander F. Schier, and Florian Engert. Escape Behavior Elicited by Single, Channelrhodopsin-2-Evoked Spikes in Zebrafish Somatosensory Neurons. *Current biology : CB*, 18(15):1133–1137, August 2008.

[13] George Gabriel Stokes. XXX. On the change of refrangibility of light. *Philosophical Transactions of the Royal Society of London*, 142:463–562, January 1852. Publisher: Royal Society.

[14] *Phenomena of Optical Metamaterials.* Elsevier, 2019.

[15] Tatjana Gric and Ortwin Hess. Chapter 8 - Active Optical Metamaterials. In Tatjana Gric and Ortwin Hess, editors, *Phenomena of Optical Metamaterials*, Micro and Nano Technologies, pages 187–261. Elsevier, January 2019.

[16] Pranab Dey. Fluorescence and Confocal Microscope: Basic Principles and Applications in Pathology. In Pranab Dey, editor, *Basic and Advanced Laboratory Techniques in Histopathology and Cytology*, pages 245–252. Springer, Singapore, 2018.

[17] Michael J. Sanderson, Ian Smith, Ian Parker, and Martin D. Bootman. Fluorescence Microscopy. *Cold Spring Harbor protocols*, 2014(10):pdb.top071795, October 2014.

[18] Jeff W. Lichtman and José-Angel Conchello. Fluorescence microscopy. *Nature Methods*, 2(12):910–919, December 2005. Number: 12 Publisher: Nature Publishing Group.

[19] Extraction, Purification and Properties of Aequorin, a Bioluminescent Protein from the Luminous Hydromedusan, Aequorea - Shimomura - 1962 - Journal of Cellular and Comparative Physiology - Wiley Online Library.

[20] The Nobel Prize in Chemistry 2008.

[21] Atsushi Miyawaki, Juan Llopis, Roger Heim, J. Michael McCaffery, Joseph A. Adams, Mitsuhiko Ikura, and Roger Y. Tsien. Fluorescent indicators for Ca 2+ based on green fluorescent proteins and calmodulin. *Nature*, 388(6645):882–887, August 1997. Number: 6645 Publisher: Nature Publishing Group.

[22] Principles of Optics | ScienceDirect.

[23] Peter M. Eimon, Mostafa Ghannad-Rezaie, Gianluca De Rienzo, Amin Allalou, Yuelong Wu, Mu Gao, Ambrish Roy, Jeffrey Skolnick, and Mehmet Fatih Yanik. Brain activity patterns in high-throughput electrophysiology screen predict both drug efficacies and side effects. *Nature Communications*, 9(1):219, January 2018. Number: 1 Publisher: Nature Publishing Group.

[24] Bonifasius Putera Sampurna, Gilbert Audira, Stevhen Juniardi, Yu-Heng Lai, and Chung-Der Hsiao. A Simple ImageJ-Based Method to Measure Cardiac Rhythm in Zebrafish Embryos. *Inventions*, 3(2):21, June 2018. Number: 2 Publisher: Multidisciplinary Digital Publishing Institute.

[25] Minsky Marvin. Microscopy apparatus, December 1961.

[26] Mojmír Petráň, Milan Hadravský, M. David Egger, and Robert Galambos. Tandem-Scanning Reflected-Light Microscope*. *JOSA*, 58(5):661–664, May 1968. Publisher: Optical Society of America.

[27] High Speed | Yokogawa America.

[28] Kang-Bin Im, Sumin Han, Hwajoon Park, Dongsun Kim, and Beop-Min Kim. Simple high-speed confocal line-scanning microscope. *Optics Express*, 13(13):5151–5156, June 2005. Publisher: Optical Society of America.

[29] Jinwoo Lee, Yukihiro Miyanaga, Masahiro Ueda, and Sungchul Hohng. Video-Rate Confocal Microscopy for Single-Molecule Imaging in Live Cells and Superresolution Fluorescence Imaging. *Biophysical Journal*, 103(8):1691–1697, October 2012.

[30] ORCA-Fusion Digital CMOS camera C14440-20UP.

[31] ORCA-Lightning Digital CMOS camera C14120-20P.

[32] Tom Vettenburg, Heather I. C. Dalgarno, Jonathan Nylk, Clara Coll-Lladó, David E. K. Ferrier, Tomáš Čižmár, Frank J. Gunn-Moore, and Kishan Dholakia. Light-sheet microscopy using an Airy beam. *Nature Methods*, 11(5):541–544, May 2014. Number: 5 Publisher: Nature Publishing Group.

[33] Eric Betzig. Excitation strategies for optical lattice microscopy. *Optics Express*, 13(8):3021–3036, April 2005. Publisher: Optical Society of America.

[34] Marc Levoy Levoy, Ren Ng, Andrew Adams, Mathew Footer, and Mark Horowitz. Light field microscopy | ACM SIGGRAPH 2006 Papers.

[35] Matthew B. Bouchard, Venkatakaushik Voleti, César S. Mendes, Clay Lacefield, Wesley B. Grueber, Richard S. Mann, Randy M. Bruno, and Elizabeth M. C. Hillman. Swept confocally-aligned planar excitation (SCAPE) microscopy for high-speed volumetric imaging of behaving organisms. *Nature Photonics*, 9(2):113–119, February 2015. Number: 2 Publisher: Nature Publishing Group.

[36] Three-dimensional virtual refocusing of fluorescence microscopy images using deep learning | Nature Methods.

[37] Sebastián A. Romano, Thomas Pietri, Verónica Pérez-Schuster, Adrien Jouary, Mathieu Haudrechy, and Germán Sumbre. Spontaneous Neuronal Network Dynamics Reveal Circuit's Functional Adaptations for Behavior. *Neuron*, 85(5):1070–1085, March 2015.

[38] Emiliano Marachlian, Lilach Avitan, Geoffrey J. Goodhill, and Germán Sumbre. Principles of Functional Circuit Connectivity: Insights From Spontaneous Activity in the Zebrafish Optic Tectum. *Frontiers in Neural Circuits*, 12, 2018. Publisher: Frontiers.

[39] Rong-wei Zhang, Xiao-quan Li, Koichi Kawakami, and Jiu-lin Du. Stereotyped initiation of retinal waves by bipolar cells via presynaptic NMDA autoreceptors. *Nature Communications*, 7(1):12650, September 2016. Number: 1 Publisher: Nature Publishing Group.

[40] Yichen Wu, Yair Rivenson, Hongda Wang, Yilin Luo, Eyal Ben-David, Laurent A. Bentolila, Christian Pritz, and Aydogan Ozcan. Three-dimensional virtual refocusing of fluorescence microscopy images using deep learning. *Nature Methods*, 16(12):1323–1331, December 2019. Number: 12 Publisher: Nature Publishing Group.

[41] Ahmed S. Abdelfattah, Takashi Kawashima, Amrita Singh, Ondrej Novak, Hui Liu, Yichun Shuai, Yi-Chieh Huang, Luke Campagnola, Stephanie C. Seeman, Jianing Yu, Jihong Zheng, Jonathan B. Grimm, Ronak Patel, Johannes Friedrich, Brett D. Mensh, Liam Paninski, John J. Macklin, Gabe J. Murphy, Kaspar Podgorski, Bei-Jung Lin, Tsai-Wen Chen, Glenn C. Turner, Zhe Liu, Minoru Koyama, Karel Svoboda, Misha B. Ahrens, Luke D. Lavis, and Eric R. Schreiter. Bright and photostable chemigenetic indicators for extended in vivo voltage imaging. *Science*, 365(6454):699–704, August 2019. Publisher: American Association for the Advancement of Science Section: Report.

[42] Ahmed S. Abdelfattah, Rosario Valenti, Jihong Zheng, Allan Wong, Kaspar Podgorski, Minoru Koyama, Douglas S. Kim, and Eric R. Schreiter. A general approach to engineer positive-going eFRET voltage indicators. *Nature Communications*, 11(1):3444, July 2020. Number: 1 Publisher: Nature Publishing Group.